


Fluidic control of a precessing axisymmetric body by near-wake coupling

Thomas J. Lambert, Bojan Vukasinovic ^{*}, and Ari Glezer 

*Woodruff School of Mechanical Engineering, Georgia Institute of Technology,
Atlanta, Georgia 30332-0405, USA*



(Received 8 March 2023; accepted 28 March 2024; published 3 May 2024)

The angular motion of a forebody-gimbaled axisymmetric cylindrical bluff body wind tunnel model that is free to pitch, yaw, and roll in a uniform stream in response to flow-induced aerodynamic loads is modified by fluidic actuation of its near wake. The model is anchored at its leading edge by a low-friction gimbal coupling attached to a wire-mounted short streamwise sting where each of the eight support wires is connected to a servo actuator for position and attitude control of the sting. Aerodynamic moments on the model and thereby its angular motions are controlled in a closed loop using fluidic modification of its near wake by azimuthally segmented flow attachment over its aft end. Actuation is effected using fourfold symmetrically distributed and independently activated synthetic jet actuators. Coupled effects of actuation-induced transitory changes in the attitude of the model are measured by an image-tracking system and the evolution of the near wake captured using high-speed stereo particle image velocimetry (SPIV). Dynamic mode decomposition (DMD) of the time-dependent near-wake flow field indicates that suppression or amplification of the natural oscillations of the model are associated with controlled changes in the symmetry and spectral content of the primary dynamic modes. It is shown that these controlled wake interactions can be harnessed to tune the temporal attitude response of the model, with natural oscillation suppression of $> 50 - 65\%$ in pitch and $75-85\%$ in yaw across the entire investigated range of Reynolds numbers of 1.32×10^5 to 1.92×10^5 . In addition, an example of amplification of the natural oscillations of $> 150\%$ is illustrated at a Reynolds number of 1.62×10^5 .

DOI: [10.1103/PhysRevFluids.9.053904](https://doi.org/10.1103/PhysRevFluids.9.053904)

I. INTRODUCTION

Axisymmetric bodies, with their axes nominally aligned to oncoming flow, impose an adverse pressure gradient to the flow along their aft surfaces, which causes the flow to sharply separate and form an open wake that has been studied for spheres [1–3], disks [4,5], cones [6,7], and cylinders with forebodies [8,9]. This resulting wake can, in the time-averaged sense, maintain axisymmetry within certain ranges of Reynolds numbers, implying the absence of a net time-averaged aerodynamic radial force on such bodies. Even with such mean-flow symmetry, these wake flows are quite complex, often characterized by spatial and temporal variations imposing nonzero momentary radial (and other) aerodynamic forces. Typically, several disparate time scales are associated with such wakes, ranging from the shortest, associated with the separating shear layers, to the longest, attributed to instability of the near-body recirculating wake domain, and the wake instability time scales are typically in between these two [2]. Several studies have been primarily focused on understanding the flow topology and dynamics of the wake of stationary

^{*}bojan.vukasinovic@me.gatech.edu

axisymmetric bodies over Reynolds number (Re)-dependent flow regimes. As can be expected, the wake complexity progresses with increasing Re , often as a result of successive bifurcations of the wake states (e.g., for an axisymmetric bluff body [9] and for a sphere and a disk [10]). Recently, detailed tomographic particle image velocimetry (PIV) measurements [3] were utilized to reconstruct the three-dimensional (3D) vortex topology of the wake of a stationary sphere, across several bifurcations with Re_D , addressing the characteristic turbulent properties of the ensuing wakes and suggesting the recirculating wake extent as the most relevant scale.

Other studies focus on the means of altering the natural flow states about such axisymmetric bodies, which are either stationary or undergoing independently controlled rigid motions (i.e., a state for which a body cannot couple and respond to altered flow field dynamics and their resulting induced aerodynamic loads). An approach in achieving this goal was motivated by the wake stability studies that pointed out the existence of the local absolute instability in the wake of axisymmetric bodies that is responsible for its large-scale unsteadiness [11,12]. The objective of these efforts was to remove this instability source by controlled modification of the base flow. For instance, Sevilla and Martínez-Bazán [13] investigated stability of the flow behind an axisymmetric body and reported suppression of vortex shedding past a critical base bleed coefficient, which was attributed to sufficient modification of the base flow that removed the absolute instability region. Meliga *et al.* [14] also considered stability analysis of the compressible flow past a slender axisymmetric body, with an objective of controlling the instability of the dominant helical modes. They showed that controlled modification of the base flow—which can be done by the mass flow, momentum, or a heat source—can be utilized to bypass instability and suppress low-frequency and high-amplitude wake unsteadiness. Recently, a numerical investigation [15] contrasted application of high- and low-frequency wake control behind a stationary axisymmetric body, pointing out opposing effects, where low-frequency actuation lowers the base pressure and increases flow unsteadiness.

Another objective in these prior modifications of the axisymmetric body wakes was direct aerodynamic force modification, such as drag reduction, which often involved flow vectoring or attachment along the circumference of the aft end of an axisymmetric body. In one of the earlier examples of this strategy, Freund and Mungal [16] achieved up to a 30% decrease in the aerodynamic drag of an axisymmetric body by induced flow attachment along its aft end using steady, circumferential blowing over an extended Coanda surface. Lo *et al.* [17] investigated the wake past an axisymmetric center body within a conical diffuser and reported an increase in the base pressure coefficient of this center body when the aft flow control was capable of eliminating the near-wake recirculating flow. Oxlade *et al.* [18] also reported the reduction in pressure drag due to suppressed wake entrainment by the trains of small-scale vortices imposed at the aft end of an axisymmetric body. A different type of aerodynamic force modification by inducing a net radial force on an axisymmetric body through an azimuthal array of four synthetic jets was demonstrated by Abramson *et al.* [19], who demonstrated various modes of wake modifications behind a stationary axisymmetric body. Lambert *et al.* [20] applied this azimuthal synthetic jet strategy to an axisymmetric body controlled in rigid dual angular periodic motion at various frequencies, primarily motivated by enhancement or suppression of the associated motion-induced wake asymmetries and consequently the net aerodynamic radial force and corresponding aerodynamic moments. Their work was also extended to demonstrate controlled enhancement or suppression of rigid periodic pitch-induced wake asymmetries in the far wake [21].

The least investigated and the most relevant to this paper are scenarios when the axisymmetric body is not fully decoupled from the changing aerodynamic loads and can consequently respond to them. However, an inherent difficulty with experimental investigations of even partially unconstrained models is related to their mounting and support in the test section of a wind tunnel. Hence, some of the prior investigations executed full free flight tests outside of the laboratory setting, such as McMichael *et al.* [22], who exploited a synthetic jet flow control approach to an axisymmetric spin-stabilized projectile to effect aerodynamic steering loads that were sufficient to steer the projectile by $\sim 30^\circ$ in a flight test. This control approach was also used in the numerical investigations by Sahu and Heavey [23], who computed the aerodynamic loads and the unsteady

asymmetric flow field around the axisymmetric projectile. Numerical work [24] extended this concept to a high-subsonic flow regime (up to a Mach number Ma of 0.9), showing comparable net-generated normal forces for both stationary and spinning models. Tethering wind tunnel models were also utilized in prior investigations for allowing the response of a model to aerodynamic loads. Detailed spatiotemporal characterization of the flow coupling with a tethered sphere was done experimentally by van Hout *et al.* [25], who identified three bifurcation regions, each of them exhibiting unique vortical compositions. Subsequently, van Hout *et al.* [26] demonstrated that acoustic excitation at a varying excitation frequency can either amplify or suppress vortex induced vibrations of tethered spheres. In a different approach to a model support, Lambert *et al.* [27] experimentally studied natural and controlled axisymmetric body responses unconstrained only in yaw, in one degree of freedom (1-DOF). They demonstrated that closed-loop control through two opposing synthetic jets positioned on the aft of an axisymmetric body along the plane of the yawing motion was capable of either enhancing or suppressing the natural instability oscillations by up to 90%. Boujo and Cadot [28] considered an unconstrained 1-DOF rotational motion as well, of a circular disk, and established the angular deflection of the disk as a linear harmonic oscillator forced by the base aerodynamic moment. It should also be noted that a large body of work concerns 1-DOF transverse oscillations of cylindrical bodies in response to the flow perpendicular to their axes, but these dynamic systems represent a separate class of problems that are not considered in this paper, and the reader is directed to review articles that address such 1-DOF vortex-induced vibrations [29,30].

In this paper, we consider the reciprocal dynamics of separated flows coupled to an axisymmetric bluff body whose axis is nominally aligned with the flow direction and supported such that it is free to precess in three degrees of freedom (3-DOF): pitch, yaw, and roll. Flow separation off the aft end of the body results in an unsteady wake that couples to the aerodynamic moments on the body, leading to natural time-dependent excursions in the angular orientation of the body. In this paper, we focus on active modification of the coupling between an axisymmetric bluff body and its near wake using four independently controlled aft-mounted synthetic jet actuators to suppress or alternatively enhance the flow-induced unsteadiness of the body, with or without a controlled imposition of a time-averaged directional body attitude. Specifically, a primary objective of this paper is to investigate the receptivity of the coupled body/wake motion to near-wake flow control, with a goal of a controlled body attitude trajectory alternative to the natural response of the body to the flow.

II. EXPERIMENTAL SETUP AND PROCEDURES

The model utilized in this paper is a scale model of the configuration that was used to demonstrate the effectiveness of flow control for steering during spin-stabilized flight [22]. The present scaled-up wind tunnel model ($D = 90$ mm, $c = 165$ mm, Fig. 1) is connected to a short sting attachment that supports an inner gimbal mount through the nose section and enables a free 3-DOF rotational response to aerodynamic pitch, yaw, and roll moments. To this end, the nose section comprises a stereolithographed thin outer shell that houses a central bearing and a counterweight that is connected to the moving model, as shown in Fig. 1(a). The bearing mounting point is designed for the equilibrium in roll, pitch, and yaw of the model (equal mass front-back and left-right due to the counterbalance in the nose). The design and construction of the moving nose elements placed specific attention on minimizing mounting friction and shell interference. The bearing is placed at $x_o = 0.25c$ downstream of the nose and upstream of the static center of pressure on this model ($x_{cp} \approx 0.33c$). The aft end of the model is shown in Fig. 1(b). The actuation jets in this model are referred to as jets 1–4 and rotate with the model roll angle. It should be noted that the equilibrium orientation of the model in roll is such that the default orientation of the jets is fully characterized by the jet 1 orientation being $\sim 35^\circ$ from vertical [the depiction in Fig. 1(b) at this angle is denoted as roll zero]. This is likely caused by the imperfections in balancing of the azimuthal model weight distribution. Consequently, none of the control jets is aligned with either of the primary directions,

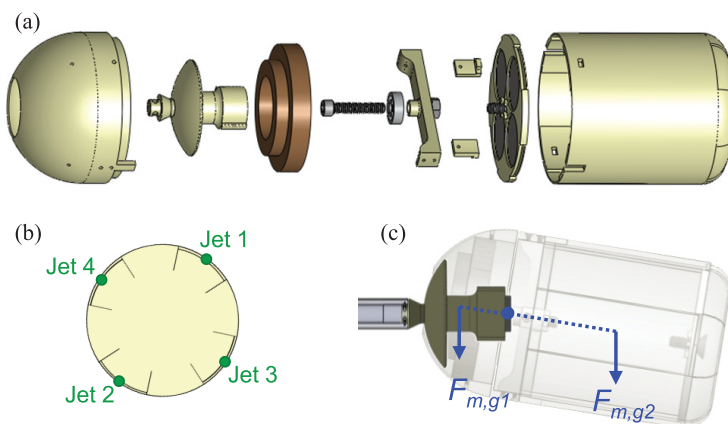


FIG. 1. Deconstructed view of (a) the three degrees of freedom (3-DOF) model components, (b) upstream view of the centered wind tunnel model with four synthetic jets marked in green, and (c) a depiction of the counterbalanced model mounted through the inner nose piece.

and moreover, the equilibrium in roll is not aligned with any of the mounting wire directions either. The inner central nose segment of the model is stationary and connected to the sting mount, as shown in Fig. 1(c), and this coupled system has realized angular ranges of motion in pitch, yaw, and roll of $\pm 16^\circ$, $\pm 18^\circ$, and $\pm 180^\circ$, respectively. The center of gravity of each of the components of the model upstream and downstream of the bearing is placed along the axis of symmetry so that it can reach moment equilibrium at any angle of pitch or yaw (marked in blue).

The flow control actuation used on this model consists of four independently driven and identical synthetic jet actuators, which are equally distributed along the perimeter of the tail section and are used to effect local aerodynamic interactions with crossflow resulting in local flow vectoring and attachment. Each synthetic jet actuator [shown in Fig. 2(a)] is issued in the streamwise direction with an orifice (height $h_j = 0.38$ mm) placed at the bottom of a backward-facing step of height $h_s = 1.5$ mm to the circumference, extending into a Coanda surface (radius $R_C = 12.7$ mm) that are based on the design of Rinehart [31]. The aft segment contains a streamwise recess downstream of the orifice edge which bounds the jet over a segmented arc [Fig. 2(b)]. Jet actuation leads to the partial attachment of an azimuthal segment of the separating shear layer at the aft end of the model along the Coanda surface and turns the outer flow into the wake resulting in an aerodynamic reaction force, normal to the centerline of the jet, and its accompanying moment. The synthetic jet actuators

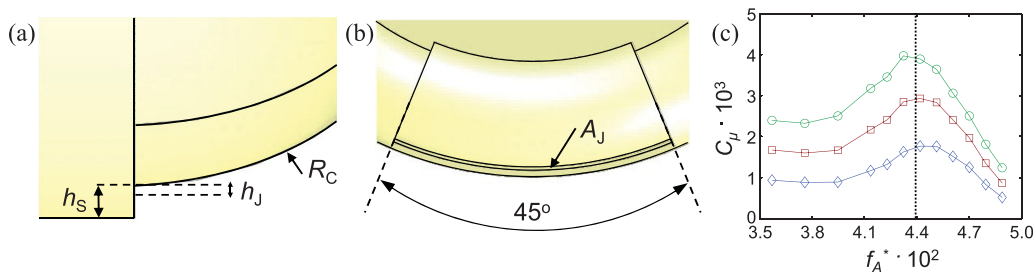


FIG. 2. (a) Top and (b) aft views of a single synthetic jet actuator orifice and (c) a variation of the jet momentum coefficient with the actuation carrier frequency for the power input $P_A^* \times 10^3 = 2$ (\diamond), 3.3 (\square), and 4.6 (\circ). The selected carrier frequency is marked by the dashed line.

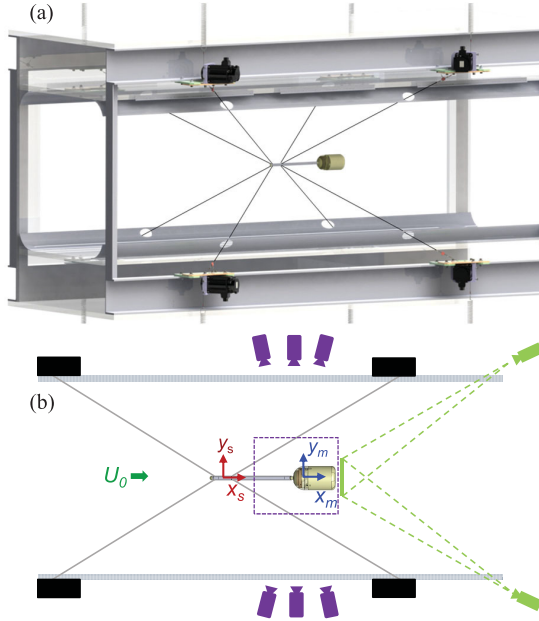


FIG. 3. (a) Six degrees of freedom traversing mechanism utilizing eight servo actuators and support wires to an upstream sting and (b) a top view schematic of the sting-mounted model, along with the high-speed stereo particle image velocimetry (SPIV) interrogation region (light green), and motion analysis system (purple).

are calibrated over a wide range of actuation frequencies f_A and applied powers P_A . The actuation frequency is scaled by the hydraulic diameter of the jet ($\sim 2h_j$) and the free stream velocity $f_A^* = 2f_A h_j / U_o$, where the actuation convective time scale is $2h_j / U_o = 19 \mu\text{s}$, and the actuation power is scaled as $P_A^* = 24P_A / (\pi \rho U_o^3 D^2)$. The jet actuators are calibrated using hot-wire anemometry in a test stand where the time-resolved velocity of the jet is measured at the center of each of the actuator orifices yielding a rectified time-periodic waveform representing alternate suction and expulsion during the jet formation. The peak of the expulsion velocity U_j is recorded over a frequency range of $0.035 < f_A^* < 0.050$ at excitation powers of $P_A^* \times 10^3 = 2.0, 3.3, \text{ and } 4.6$. The variation of the jet momentum coefficient $C_{\mu} = (4U_j^2 A_j) / (\pi U_o^2 D^2)$, with f_A^* , is shown in Fig. 2(c), and it is used to select the actuation carrier frequency in this paper, on the order of $f_{\text{act}} \sim 1 \text{ kHz}$.

The sting that supports this model is wire mounted in an $0.91 \times 0.91 \text{ m}$ open-return wind tunnel, and tests are conducted at free stream speeds U_o of up to 30 m/s ($\text{Re}_D = 1.92 \times 10^5$). The traverse support mechanism utilizes 8 stranded (0.6-mm-diameter) support wires to control the sting position within the test section of the wind tunnel with minimal aerodynamic interference and is shown in Fig. 3(a). This wind tunnel traverse has been used for a variety of different geometries and studies [20,21,32] and is characterized in detail by Lambert *et al.* [33]. The position and orientation of the suspended sting follows a prescribed trajectory using independently controlled servo motor actuators that are mounted outside the test section of the tunnel and also uses in-line load cell sensors in each mounting wire as feedback and measurement signals (for reference, the control approach is discussed in detail in Appendix). Figure 3(b) shows a view of the experimental setup from above. The coordinate system that is used for the motion of the sting (in red, x_s, y_s) and the model (in blue, x_m, y_m), where the vertical directions are out of the page (z_s, z_m), such that the coordinate frame is right handed, and the angles of attack are defined: α_x roll about the x axis, α_y pitch about the y axis, and α_z yaw about the z axis. The 16-mm-diameter sting is 30.5 mm long, and the center of the wire mounts are placed 225 and 280 mm upstream of the model nose, and the wire mounting locations on the sting form angles of 105° and 75° with respect to the y and z axes. The mass of the

model is 625 g, and in the absence of air flow, it exerts a moment of 1.83 N m on the traverse. The attitude of the sting is controlled by the traverse, and in the base position, its attitude is designed to coincide with the direction of the free stream. The electrical wires for the flow control synthetic jets are weaved along the back four support wires of the sting and along the sting, and the support wires and sting provide electrical ground. It is important to emphasize that there are two independent controllers in this paper (both discussed in Appendix): the controller that adjusts the mounting wires of the sting to hold the prescribed attitude/trajectory of the sting and a controller that adjusts the jet momentum coefficient amplitude to the four synthetic jets of the model to control the trajectory of the model. The intended purpose of the controlled sting is to hold the center of rotation of the model stationary regardless of flow-induced loads (when desired). Toward the end of this work, the sting control by support wires commands the center of rotation of the model in a prescribed fashion for demonstration that the flow control (jets) can successfully interact with the wake even when the sting support is nonstationary. In this paper, our primary focus is on the controller that controls the model-wake coupling through adjustments to the jet momentum coefficients.

An external six-camera, high-speed (600 fps) VICON MX motion analysis tracking system measures the motion of the model in 3-DOF and is simultaneously used for extracting the pitch and yaw of the sting, depicted in purple in Fig. 3(b). Each camera has a 12.5 mm lens and a resolution of 4 megapixels and is interfaced to a host computer. A software image analysis extracts the 3-DOF of the body ($\alpha_{x,m}$, $\alpha_{y,m}$, and $\alpha_{z,m}$) and the 6-DOF of the sting (x_s , y_s , z_s , $\alpha_{x,s}$, $\alpha_{y,s}$, and $\alpha_{z,s}$) based on a set of infrared (IR) markers on the sting and model. The software calibration, prior to each set of experiments, yields typical uncertainties of each IR marker location on the order of 0.25–0.5 mm in each direction, which are equivalent to uncertainty of <0.2 mm in x_s , y_s , and z_s , and $<0.1^\circ$ in α_x , α_y , and α_z for both the sting and the model. In addition, the velocity in the wake is measured using a high-speed stereo PIV (SPIV) system, as shown schematically in a top view in Fig. 3(b). This SPIV system includes two cameras, each at an angle of 25° (shown in green) which resolve all three components of the velocity field (U_x , U_y , U_z) in an interrogation region downstream of the aft end of the model (x , y , z). The interrogation region is placed in the $y-z$ plane at $x/c = 0.9$ (or $0.25D$ downstream of the aft end of the model), spanning $1.8D$ in y and in z ($y = \pm 0.9D$ and $z = \pm 0.9D$, centered about the streamwise axis of the gimbal of the model). The high-speed SPIV system records image pairs separated by $\Delta t = 32 \mu\text{s}$ at 500 Hz. The images are processed using commercial software (LaVision) over the 24×24 pixel SPIV interrogation region. Initial image preprocessing involved subtracting off a background image and applying a mask over the body surfaces, when present in the view. The cross-correlation algorithm is applied in multiple passes, each with 50% overlap. The output vector matrix of a single measurement domain consisted of 55×55 vectors, yielding a spatial resolution of 3.3 mm in Δy and Δz . Primarily due to the time-varying nature of the particle seeding and partially due to the vector rejections, not all instantaneous velocity matrices have a complete 3025 vectors. After capturing the instantaneous vector fields of each recorded set (typically 5 s, an equivalent of 2500 image pairs), a proper orthogonal decomposition (POD) algorithm is utilized for completion of the 55×55 vector sets for each instant in time using a reconstruction of the vector field with the first 20 POD modes as $\vec{X}_{\text{reconstructed}}(t) = \langle \vec{X} \rangle + \sum_{n=1}^{20} \lambda_n(t) \cdot \vec{\varphi}_n$, where $\langle \vec{X} \rangle$ is the time averaged value of $\vec{X}(t)$, $\vec{\varphi}_n$ is the n th POD mode, $\lambda_n(t)$ is the weighted time coefficient of the n th POD mode. The uncertainties of the SPIV measurements are estimated as the upper bounds, based on the root mean square (RMS) variation of the instantaneous velocity vectors. Specifically, the RMS velocity error is divided by the reconstructed average absolute value of the velocity magnitude at each space and averaged over all the spatial vectors leading to a velocity uncertainty estimate of $\sim 4.9\%$. It should be emphasized that this is an upper bound of uncertainty, as it also incorporates any turbulent RMS or any other physical wake dynamics that would increase RMS. The SPIV vorticity about the streamwise direction (ζ_x) is calculated from a finite difference stencil in space, using the measured velocities U_y , U_z , Δy , and Δz (where $\zeta_x \sim \Delta U_z / \Delta y - \Delta U_y / \Delta z$). Using this upper bound of 4.9% on uncertainty in velocity measurements and assuming an upper bound of 8.3% uncertainty in the grid spacing (or 1 pixel out

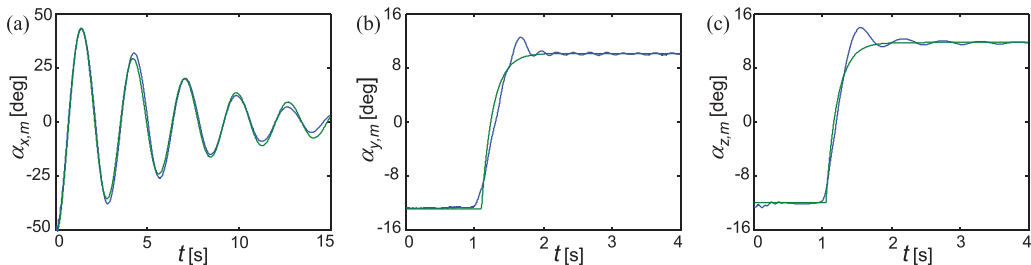


FIG. 4. Realized perturbations of the model in (a) roll, (b) pitch, and (c) yaw, shown in blue, and best fits to a mass-spring-damper model shown in green.

of 12 pixels difference between two grid points), the uncertainty in vorticity is estimated to have an upper bound of $\sim 15\%$.

III. MODELING OF THE PRECESSING BODY DYNAMICS

The model dynamics are estimated as a combination of second-order mass-spring-damper systems with spring constant K_x , damping constants C_x and C_{yz} , inertias I_x and I_{yz} , and external roll, pitch, and yaw moments (M_R , M_P , M_Y):

$$I_x \ddot{\alpha}_x + C_x \dot{\alpha}_x + K_x \alpha_x = M_R(t), \quad I_{yz} \ddot{\alpha}_y + C_{yz} \dot{\alpha}_y = M_P(t), \quad I_{yz} \ddot{\alpha}_z + C_{yz} \dot{\alpha}_z = M_Y(t). \quad (1)$$

This model excludes any friction effects caused by the bearing and assumes that the system responds symmetrically in pitch and yaw (with the same damping and inertia) and that these parameters are independent of the roll dynamics (which have separate damping, inertia, and spring constants). Within the entire range of realizable pitch and yaw angles, the model can be in equilibrium, and therefore, the spring constant in pitch and yaw is considered negligible (otherwise, the model would restore to center). As noted in the discussion of Fig. 1, there is only one equilibrium point at roll defined as the roll-zero angle [and shown in Fig. 1(b)] which persists in the absence of flow and external moments. The damping and spring constant in roll are estimated from the model released at an initial roll angle set to $\alpha_x = -50^\circ$, shown in Fig. 4(a) in blue. The model is released at $t = 0$, where the spring constant causes the model to oscillate, and the damping constant reduces its kinetic energy. The response dynamics of the model to external moments in either pitch or yaw are each measured from perturbations of the model (the dynamic perturbations are measured using the motion analysis system). These perturbations are performed manually by hand and designed such that the model would start at an amplitude comparable with the expected aerodynamic vibrations ($\sim -10^\circ$), are introduced to a manual external force at $t = 1$ s, and end at the opposite amplitude ($\sim 10^\circ$), with negligible motion in the other DOFs. The corresponding measured time traces are shown in blue in Figs. 4(b) and 4(c). To estimate the dynamic parameters, the inertia components $I_x = 6.45 \times 10^{-4} \text{ Nms}^2/\text{rad}$ and $I_{yz} = 1.25 \times 10^{-3} \text{ Nms}^2/\text{rad}$ are extracted from computer-aided design software ignoring the weight of electrical wires. The measured perturbation traces in Fig. 4 in blue and their numerical derivatives are then computed and substituted into their respective DOF in Eq. (1), setting the external moments equal to zero. The result yields three sets of data points: one in roll which is used to estimate the least squares fit to K_x and C_x , one in pitch which is used to estimate the least squares fit to C_{yz} , and one in yaw which is used to produce another least squares fit to C_{yz} . The results are $K_x = 3.2 \times 10^{-3} \text{ Nm/rad}$, $C_x = 1.8 \times 10^{-4} \text{ Nms/rad}$, and $C_{yz} = 8.5 \times 10^{-3} \text{ Nms/rad}$ (C_{yz} is taken as the average of the two estimates, each with a difference of $\sim 0.2 \times 10^{-3}$ from the average). The fit to the roll dynamics is shown in Fig. 4(a) in green and is in good agreement to the measured response, with a similar frequency and decay rate. The fits to the pitch and yaw dynamics with the same damping coefficient are shown in Figs. 4(b) and 4(c), showing a reasonable agreement for $t > 1$ (for $t < 1$, the fit is replaced with $\alpha_y = 0$ or α_z at its initial condition). The least

squares fit to pitch and yaw does not capture the initial overshoot of the model, which is attributed to frictional effects in the bearing, but accurately captures the steady-state response in both pitch and yaw, even with the same damping coefficient. It is noted that Eq. (1) is not used to design the fluidic actuation control loop defined in Appendix, as this controller is agnostic of moments and is a proportional-derivative (PD) controller on pitch and yaw angles. Equation (1) is primarily used for calculating the pitching and yawing moment the model experiences presented in Secs. V and VI. In addition, this model assumes that pitch and yaw parameters are independent of roll dynamics, which is not directly tested but is validated as a reasonable assumption from data shown in Secs. IV–VI because the measured roll dynamics ($\sim 2^\circ/\text{s}$) is an order of magnitude lower than the measured pitch or yaw dynamics ($\sim 20^\circ/\text{s}$).

IV. AERODYNAMIC CHARACTERISTICS OF THE PRECESSING BODY

Prior to assessing the receptivity of the coupled body/wake motion to near-wake flow control to overcome the natural response of the body to the flow, the baseline response of the 3-DOF freely precessing (roll, pitch, and yaw) model to its interaction with the embedding flow is characterized in detail, with coordinate systems for the model, and its sting support, defined in Sec. II (cf. Fig. 3). In this paper, the Reynolds number of the model is high enough so that initial flow perturbations (e.g., by coupling to its near wake) rapidly amplify, and the model oscillates within a finite envelope of vertex angles between its centerline and the flow direction. In the present experimental setup, the mounting wires to the sting that supports the model are not spaced equally in the azimuthal direction to enable control of the roll angle of the sting, and as a result, the sting is slightly less stable in yaw than in pitch. In the absence of flow control, this slight asymmetry can contribute to the time periodic oscillations of the model to be directionally biased in yaw. However, it is also noted that, depending on the Re regime, it has been shown [34] that the (tethered) axisymmetric body coupling to its wake can have a preferential angular response. An illustration for an oscillation response is shown in Fig. 5 at $U_o = 28 \text{ m/s}$ ($\tau_{\text{conv}} = c/U_o = 5.9 \text{ ms}$, $\text{Re}_D = 1.62 \times 10^5$). Figures 5(a), 5(c), and 5(e) show an 8 s time trace of the angular positions of the model in α_x (roll), α_y (pitch), and α_z (yaw), respectively, and the corresponding spectra (frequency resolution of 0.05 Hz) are shown in Figs. 5(b), 5(d), and 5(f). Each of these traces exhibits distinct frequency and amplitude responses in roll ($f_x = 0.4 \text{ Hz}$, 0.7°), yaw ($f_z = 1.55 \text{ Hz}$, 5.2°), and pitch ($f_y = 2.90 \text{ Hz}$, 1.5°), with a characteristic baseline period that is defined off the average time of a yaw cycle: $\tau_z = 0.65 \text{ s}$ ($\sim 110\tau_{\text{conv}}$). These data show that the characteristic pitch frequency is about two times higher than the corresponding yaw frequency, and the pitch spectrum also contains a second peak at the yawing frequency. Although the support sting is commanded to be held stationary, Figs. 5(g) and 5(i) show that the sting pitch and yaw angles vary with amplitudes of 0.25° and 0.5° , respectively, and the spectra of the sting motion [Figs. 5(h) and 5(j)] contain the yaw and pitch frequencies of the model, indicating the model and sting are indeed coupled (Secs. IV and V demonstrate that this coupling can be effectively enhanced or suppressed with actuation). In this paper, we omit the sting roll angle due to its near-zero variations that are approximated as a time-invariant zero. The data for the base motion of the model are used to calculate two-dimensional (2D) probability density functions of the yaw and pitch angles over 200 s ($34000\tau_{\text{conv}}$ or $310\tau_z$) and plotted for the model [Fig. 5(k)] and sting [Fig. 5(l)]. These probability density functions show that the model undergoes its maximum pitch excursion at the extremes of the yawing angle, and its path is more exaggerated in yaw than the path of the sting [compare the scatter in Figs. 5(k) and 5(l)].

The RMS amplitudes of oscillation in roll [$\alpha_{x,\text{RMS}}$, Fig. 6(a)], pitch [$\alpha_{y,\text{RMS}}$, Fig. 6(b)], and yaw [$\alpha_{z,\text{RMS}}$, Fig. 6(c)] vary with Re_D and are shown for the sting (red) and model (blue) throughout $1.32 \times 10^5 < \text{Re}_D < 1.92 \times 10^5$ using $310\tau_z$ records. Figure 6(a) shows the roll amplitude which has the smallest excursion, approximately twice as small as the pitch response and significantly smaller than the yaw response, although it grows throughout the measured range of Re_D . Figures 6(b) and 6(c) show that the RMS of the sting pitch and yaw as well as the model pitch increase with Re_D throughout the range $1.32 \times 10^5 < \text{Re}_D < 1.92 \times 10^5$. The model yaw, however

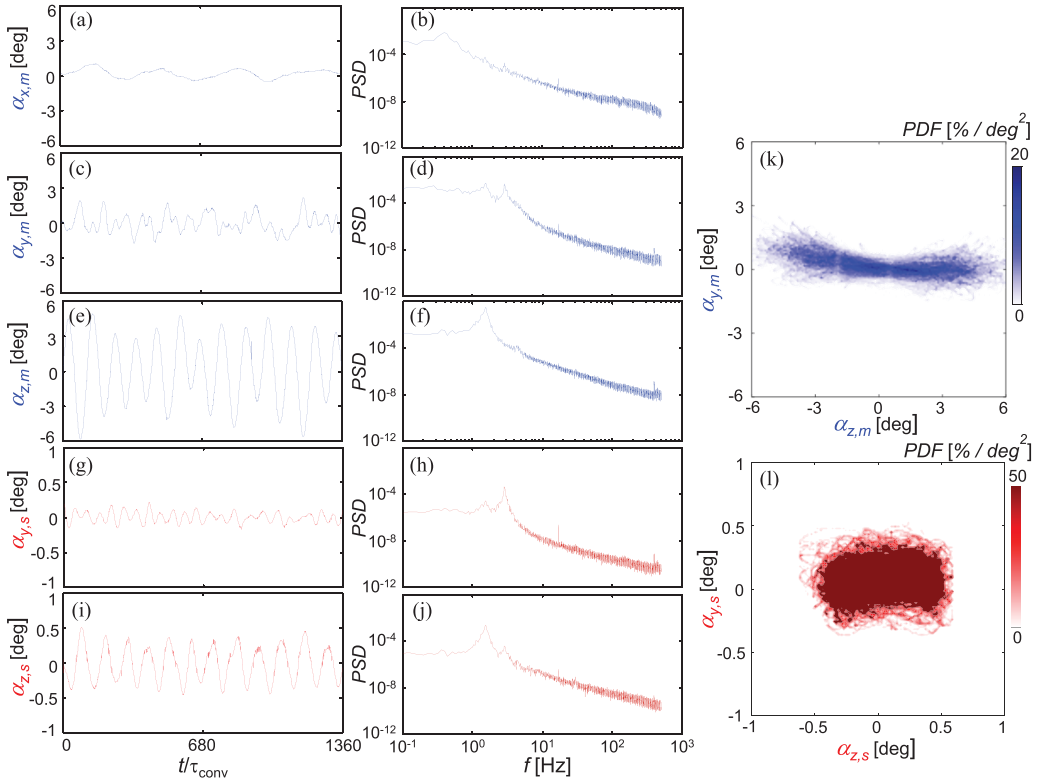


FIG. 5. Flow induced dynamics of the model (in blue) and sting (in red) at $Re_D = 1.62 \times 10^5$ for instantaneous time traces of (a) roll, (c) and (g) pitch, and (e) and (i) yaw, and (b), (d), (f), (h), and (j) their respective power spectra, along with probability density functions of the respective (k), (l) pitch and yaw over 25 measurements.

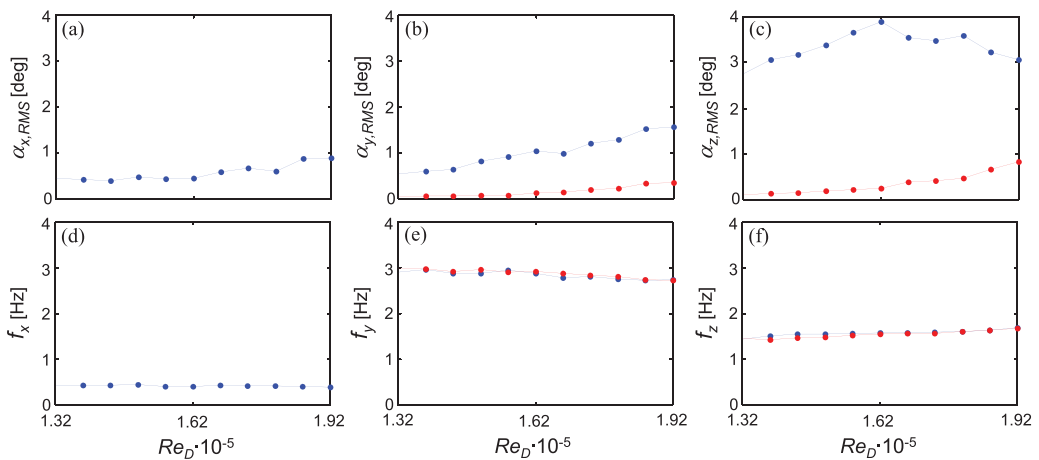


FIG. 6. Variations of the model (blue) and sting (red) (a)–(c) average root mean square (RMS) amplitude and (d)–(f) characteristic frequency in (a) and (d) roll, (b) and (e) pitch, and (c) and (f) yaw, with Reynolds number.

(the primary excursion), only increases to $Re_D = 1.62 \times 10^5$, with a maximum RMS level of 4° ($\sim 5.6^\circ$ amplitude) and then decreases to 3.1° ($\sim 4.4^\circ$ amplitude) at $Re_D = 1.92 \times 10^5$. It is interesting to note that, throughout the entire range of Re_D , the pitch-to-yaw ratio of the model increases (from 17% at 1.32×10^5 to 55% at 1.92×10^5), while the pitch-to-yaw ratio of the sting remains nearly invariant ($\sim 42\%$), indicating that the angular responses are indeed Re dependent. The corresponding variation of the characteristic frequencies (f_x, f_y, f_z), with Re_D for both the sting and model responses, are shown in Figs. 6(d)–6(f) in roll, pitch, and yaw, respectively. Figure 6(d) shows the roll excursion is ~ 6 times slower than the pitch disturbance and three times slower than the yaw disturbance. Figure 6(e) shows that the disturbance frequency of the model and the sting in pitch are the same, suggesting that the flow initially disturbs the coupled model-sting system together, and the difference in amplitude develops afterward. Figure 6(f) also shows the matching disturbance frequency between the model and sting in yaw but, in addition, shows the yawing frequency grows with Re_D [as opposed to Fig. 6(e), where the pitching frequency decays with Re_D], indicating that the disturbance frequencies in pitch and yaw are not harmonics of each other even though they differ by nearly a factor of two. Most of the remaining investigations are conducted at $Re_D = 1.62 \times 10^5$, for which the sting dynamics are considered stable and negligible (having an amplitude of $< 0.25^\circ$).

The near wake behind the unactuated model at $Re_D = 1.62 \times 10^5$ is measured using SPIV [as discussed with Fig. 3(b)] yielding a time-resolved (500 Hz) 3D velocity field including the streamwise (U_x) and cross-stream (U_y and U_z) velocity components. Following the POD reconstruction of the velocities of the flow field, the instantaneous streamwise vorticity ζ_x is reconstructed from the respective streamwise vorticity POD modes as $\delta \cdot (\frac{d\tilde{\varphi}_{n,w}}{dy} - \frac{d\tilde{\varphi}_{n,v}}{dz})$, where the derivatives are taken using a 3×3 stencil and a first-order centered analysis, and therefore, the vorticity POD modes are normalized by the grid spacing between velocity vectors δ , which is uniform in the y and z directions of all the datasets measured. Figures 7(a)–7(d) show an instantaneous reconstructed flow field with velocity components U_x [Fig. 7(a)], U_y [Fig. 7(b)], and U_z [Fig. 7(c)], and ζ_x [Fig. 7(d)] using color raster maps on a 55×55 grid. The key features in this flow field are the velocity deficit at the center of the streamwise direction [Fig. 7(a)] and inner and outer layers of cross-stream velocities of opposing senses [Figs. 7(b) and 7(c)]. Because the primary oscillation is in the yaw direction, the horizontal velocity (U_y) is typically larger in magnitude than the vertical velocity (U_z). The corresponding vorticity field [Fig. 7(d)] also has two dominant concentrations of opposing sign, although the dominant magnitudes typically coincide with the largest cross-stream velocity [compare Figs. 7(b) and 7(d)]. To characterize the time dependence of the flow behind the model (and later characterize the differences effected by the actuation), four-second time traces of u, v, w , and ζ_x along the y axis [$-0.75 < y/D < 0.75$ and $z/D = 0$ in Figs. 7(a)–7(d)], and the z axis [$-0.75 < z/D < 0.75$ and $y/D = 0$ in Figs. 7(a)–7(d)] are shown in Figs. 7(e)–7(h) and Figs. 7(i)–7(l), respectively. The time evolution of the streamwise velocity shown in Figs. 7(e) and 7(i) shows a primary deviation in the horizontal centerline comparable with the yaw dynamics and a secondary deviation in the vertical centerline comparable with the pitch dynamics [compare Fig. 7(e) with Fig. 5(e), and Fig. 7(i) with Fig. 5(c)]. Other noteworthy features are in the horizontal centerline U_y [Fig. 7(f)] and the vertical centerline U_z [Fig. 7(k)] components, both of which have an outer layer where flow is advected toward the center, and an inner layer whose sign of oscillation depends on the pitch and yaw location of the model, where the magnitude of these regions approach 30% of the freestream speed. By comparison, these effects are smaller and more diffused in the horizontal centerline U_z [Fig. 7(g)] and vertical centerline U_y [Fig. 7(j)] although still with a periodic pattern that is aligned with model motion. An interesting feature of this wake is that the horizontal centerline vorticity has the same structure as the vertical centerline velocity even though it is measured in different locations [compare Fig. 7(k) with Fig. 7(h)], and the same holds for the horizontal velocity and vertical vorticity [compare Fig. 7(f) with Fig. 7(l)]. This suggests that part of the driving aerodynamic force that maintains the instability in the model yaw (as well as horizontal

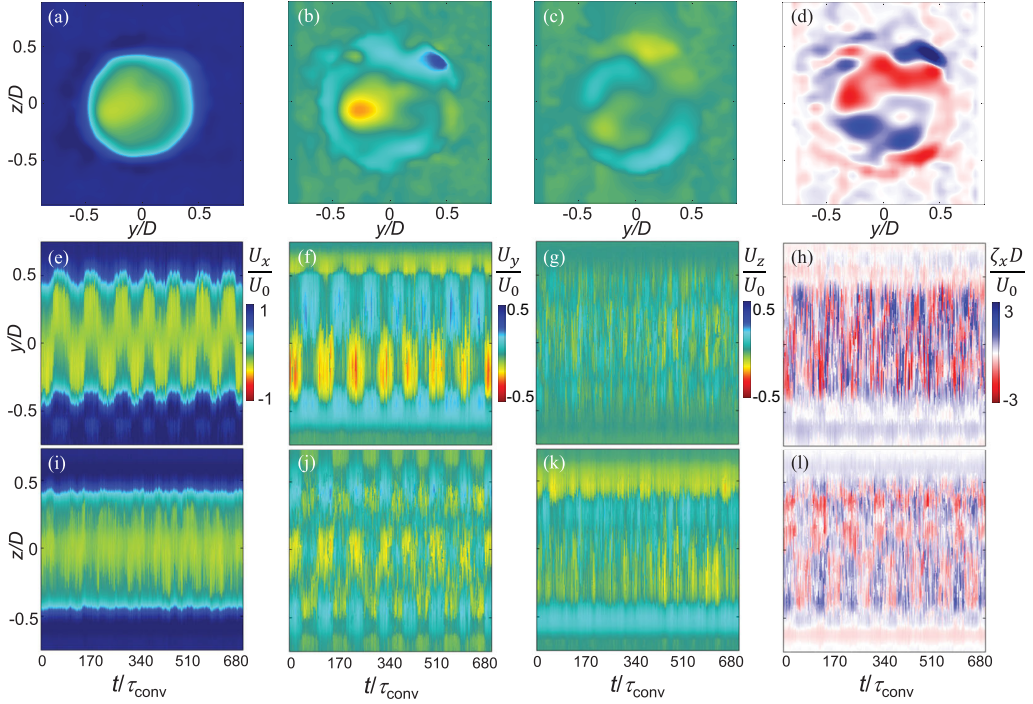


FIG. 7. An instantaneous snapshot of (a)–(d) the wake behind the unactuated model and time traces of (e)–(h) the horizontal centerline and (i)–(l) vertical centerline (a), (e), and (i) streamwise U_x and (b), (f), and (j) cross-stream U_y and (c), (g), and (k) U_z velocity components and (d), (h), and (l) streamwise vorticity ζ_x , at $Re_D = 1.62 \times 10^5$.

wake development) is induced by the structure of the streamwise vorticity concentrations in the vertical direction.

The POD modes of the subset of $\bar{\varphi}_n$ that correspond to the streamwise velocity $\bar{\varphi}_{n,u}$ are shown in Figs. 8(a)–8(g) with $n = 1 - 7$, respectively, along with the energy contribution of these modes [Fig. 8(h)] $E_n(\%) = 100|\lambda_n|^2 / \sum_{i=1}^{NN} |\lambda_i|^2$, where NN is the rank of the dataset. The first mode shown in Fig. 8(a), which represents the yaw instability in the wake, is 9% of the total energy and has ~ 3 times the energy of the next mode. The second mode [Fig. 8(b)] represents the pitch instability and is like a rotated version of the first mode, with 3% of the total energy. The next five modes [Figs. 8(c)–8(g)] have a similar structure with a central velocity contribution and two dominant external contributions which are attributed to fluctuations in the shear layer.

The cross-stream velocity modes $\bar{\varphi}_{n,v}$ and $\bar{\varphi}_{n,w}$ and their respective normalized vorticity $\bar{\varphi}_{n,\zeta}$ are plotted in Fig. 9 with the first seven modes, like Figs. 8(a)–8(g). The pairing of the first and second modes seen in the streamwise velocity in Figs. 8(a) and 8(b) is observed in the cross-stream velocities in Figs. 9(a) and 9(b), each with predominant counterrotating vorticity concentrations, where the counterrotating concentration pair in the vertical direction in Fig. 9(a) affect a larger area of the wake. In the cross-stream velocity modes, it becomes apparent that mode 3 [Fig. 9(c)] and mode 6 [Fig. 9(f)] are rotated pairs with an internal vertical structure that is centered between two external opposing vortices. Likewise, mode 4 [Fig. 9(d)] and mode 5 [Fig. 9(e)] are rotated pairs with an internal vorticity concentration that is off center from two external vorticity pairs. Modes 3–6 are associated with the shear layer dynamics, as mentioned in the discussion of Figs. 8(c)–8(g), but the cross-stream modes primarily indicate whether the flow fluctuations cross through the center of the wake [modes 3 and 6 in Figs. 9(c) and 9(f)] or are asymmetric about the center of the wake [modes

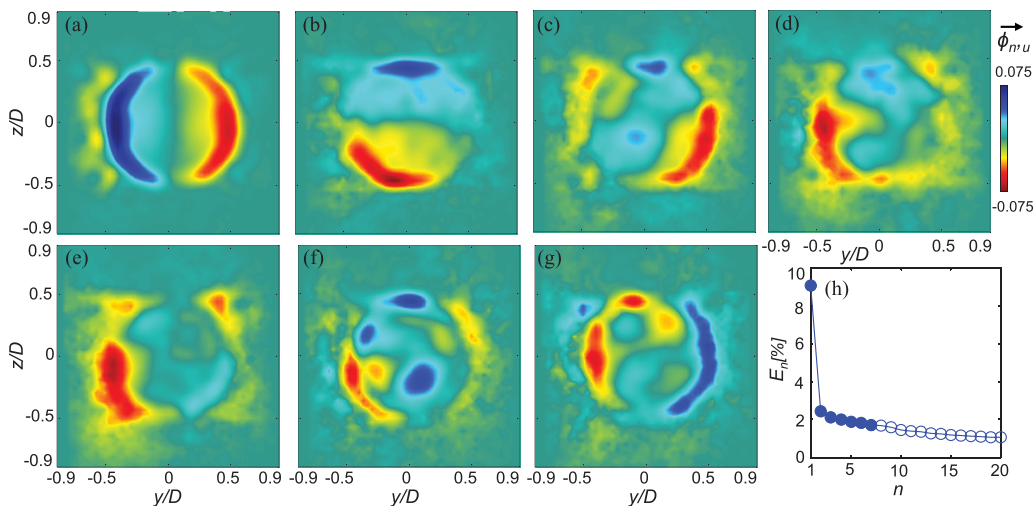


FIG. 8. Contour plots of the streamwise velocity proper orthogonal decomposition (POD) modes $\phi_{n,u}$, with mode number (a) $n = 1$, (b) $n = 2$, (c) $n = 3$, (d) $n = 4$, (e) $n = 5$, (f) $n = 6$, and (g) $n = 7$, and (h) the energy distribution of the modes for the base flow at $Re_D = 1.62 \times 10^5$.

4 and 5 in Figs. 9(d) and 9(e)]. The seventh cross-stream velocity component mode is different than the previous four modes [Fig. 9(g)], having four counterrotating vorticity pairs instead of a single one that spreads across the entire wake, and it is clear that this highest-order (lowest-energy) mode has the most broken-up structure and least organization.

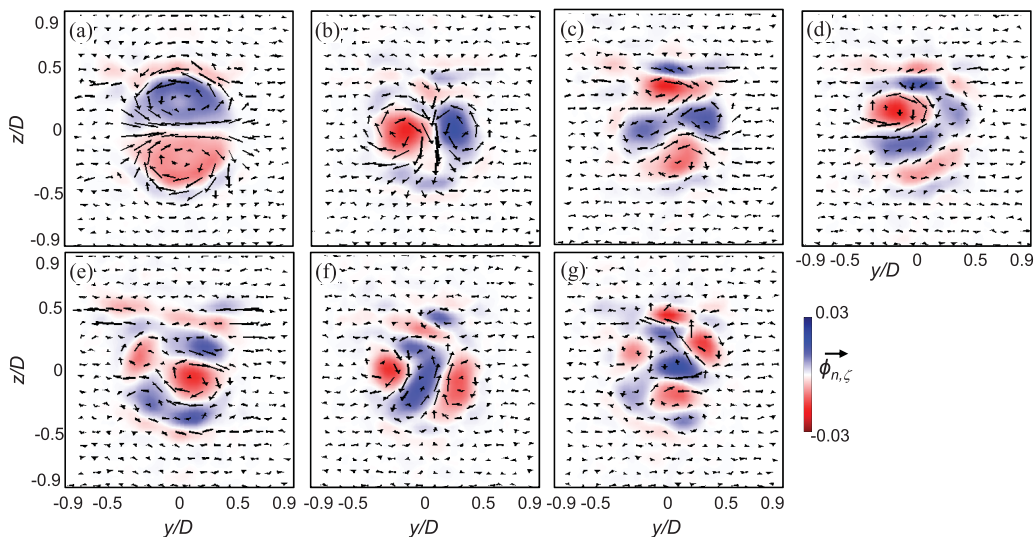


FIG. 9. Quiver plots of the proper orthogonal decomposition (POD) modes of the cross-stream velocities ϕ_v and ϕ_w , with mode number (a) $n = 1$, (b) $n = 2$, (c) $n = 3$, (d) $n = 4$, (e) $n = 5$, (f) $n = 6$, and (g) $n = 7$, colored by their streamwise vorticity $\phi_{n,\zeta}$ for the base flow at $Re_D = 1.62 \times 10^5$.

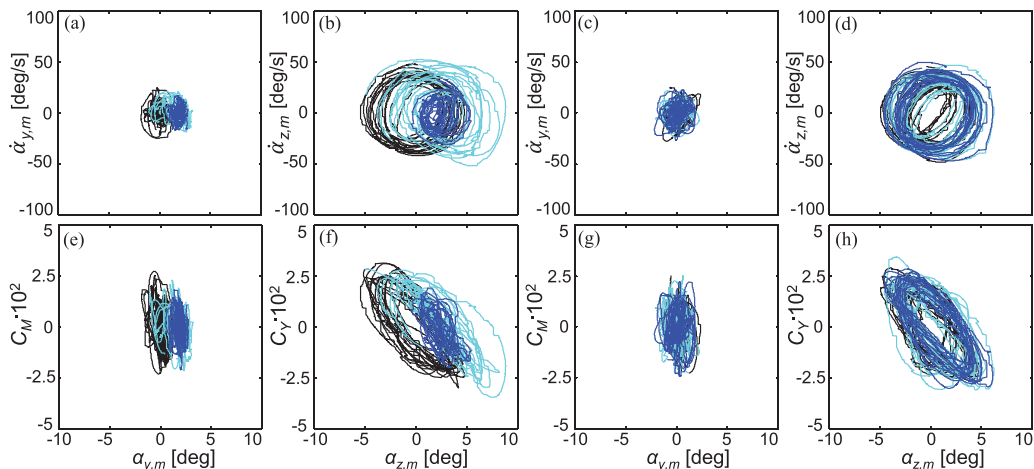


FIG. 10. Phase plots of 10 instantaneous traces of (a) and (c) the model pitch rate $\dot{\alpha}_y$, (b) and (d) yaw rate $\dot{\alpha}_z$, and moment coefficients (e) and (g) C_M and (f) and (h) C_Y , for open-loop actuation by (a), (b), (e), and (f) a single jet and (c), (d), (g), and (h) all four jets for $t/\tau_{conv} = -170$ to 0 (black), 0–170 (cyan), and 170–510 (blue) after the onset of actuation at a fixed $C_\mu = 0.003$ and $Re_D = 1.62 \times 10^5$.

V. EFFECTS OF AFT FLUIDIC ACTUATION

The effect of aft actuation is investigated at $U_o = 28$ m/s ($Re_D = 1.62 \times 10^5$) using single- or four-jet control. Clearly, in examining the sensitivity of the model response to the fluidic actuation of a single jet, the orientation of that single jet relative to the pitch and yaw plane is important, but in the case of four jets, such sensitivity is bypassed by the presence of opposing jets at the symmetric opposite angular orientation. Instantaneous pitch (α_y) and yaw (α_z) angles of the model are measured over sampling intervals of 3 s, where actuation is activated $t = 0$. The angular velocities $\dot{\alpha}_y$ and $\dot{\alpha}_z$ as well as the corresponding accelerations are computed from time series of the angles and used to compute the aerodynamic moments on the model using Eq. (1) in Sec. II. The pitch and yaw moment coefficients (C_M and C_Y) are then calculated from these moments as $C_{M,Y} = \frac{M_{y,z}}{\frac{\pi}{8} \rho U^2 D^2 c}$. Phase plots of the angular velocities and aerodynamic moments plotted against the instantaneous angle (in both pitch and yaw) are shown in Fig. 10 in three separate regimes: unactuated in black ($-170 < t/\tau_{conv} < 0$), transient in cyan ($0 < t/\tau_{conv} < 170$), and the controlled dynamics in blue ($170 < t/\tau_{conv} < 510$). Figures 10(a), 10(b), 10(e), and 10(f) show single-jet actuation, while Figs. 10(c), 10(d), 10(g), and 10(h) show four-jet actuation, with phase plots of the pitch rate [Figs. 10(a) and 10(c)], yaw rate [Figs. 10(b) and 10(d)], pitch moment [Figs. 10(e) and 10(g)], and yaw moment [Figs. 10(f) and 10(h)]. It is interesting to note that, although the motion excursion is significantly larger in yaw than in pitch, the magnitudes of the unactuated moments are similar; the maximum in the pitch moment is $\sim 80\%$ of the yaw moment without actuation. In addition, the baseline yaw moment response [Figs. 10(f) and 10(h), black trace] agrees with the yaw response of the model constrained to a free 1-DOF yaw motion [27]. Upon activating single-jet control [jet 3, where the jets are numbered in Fig. 1(b)], α_y gains a bias of 2° and decreases in the fluctuations in position and velocity of $\sim 40\%$ [Fig. 10(a)] and in its moment by $\sim 30\%$ [Fig. 10(e)]. A similar trend occurs in α_z , with a bias of 2° and decreases in fluctuations of its position and velocity of $\sim 60\%$ [Fig. 10(b)] and of its moment by $\sim 50\%$ [Fig. 10(f)]. Although the transient behavior in α_y shown in cyan is a somewhat direct transition between the unactuated and actuated states, α_z instead has a significant amount of overshoot, with a growth of amplitude from 5.5° to 7° about a bias of 2° and then a collapse into its developed amplitude of 2.5° . This transition from the unactuated flow to the new developed amplitude occurs in ~ 1 s (~ 1.5 baseline oscillation periods τ_z and 170 convective time

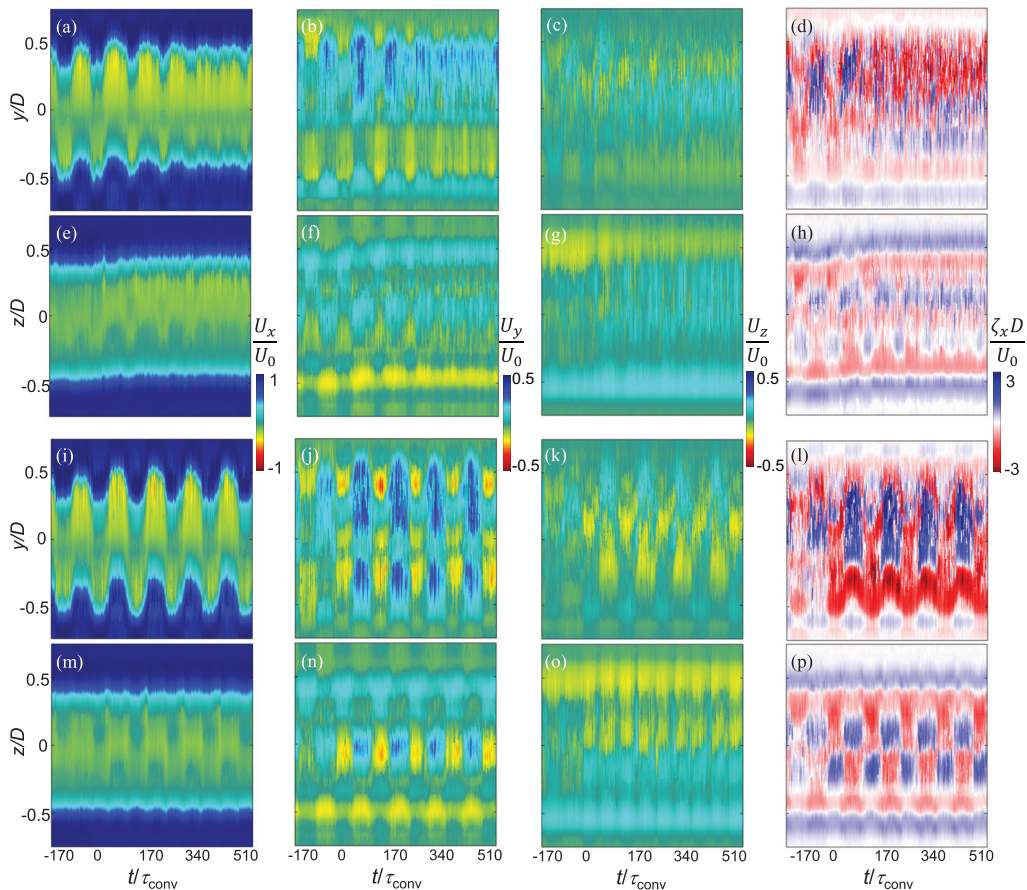


FIG. 11. The time traces of (a)–(d) and (i)–(l) the horizontal centerline and (e)–(h) and (m)–(p) vertical centerline (a), (e), (i), and (m) streamwise U_x and (b), (f), (j), and (n) cross-stream U_y and (c), (g), (k), and (o) U_z velocity components and (d), (h), (l), and (p) streamwise vorticity ζ_x for (a)–(h) the open-loop single-jet and (i)–(p) four-jet actuation applied at $t = 0$, at a fixed $C_\mu = 0.003$ and $\text{Re}_D = 1.62 \times 10^5$.

scales τ_{conv}). In contrast, four-jet actuation [Figs. 10(c), 10(d), 10(g), and 10(h)] does not have a well-defined state transition, where the actuated dynamics appear to be like the unactuated model with a slight increase of the fluctuations in α_z and $\dot{\alpha}_z$ during the transition [see Figs. 10(d) and 10(h)] and almost no changes in pitch [see Figs. 10(c) and 10(h)]. The significance of the lack of change in the system response with four-jet actuation, along with the overshoot and temporary increased vibrations with activation of an open-loop single jet, shows the need for timed actuation in controlling this free responding model, which is discussed further in the closed-loop control Sec. V. This result is unlike the two-jet control in 1-DOF [27], where suppression of the oscillation occurred, and this is presently attributed to the effects of the additional two jets (e.g., in the two-jet case for a yawing motion the reduction of yaw oscillations might be decreased if the two out-of-plane jets were activated).

The wake behind the model upon the onset of the open-loop actuations shown in Fig. 11 is analyzed using the time-dependent PIV measurements along the y and z axes of the wake, which are shown in Figs. 11(a)–11(h) and Figs. 11(i)–11(l) for single- and four-jet actuation, respectively. These data are presented in a similar fashion to Figs. 7(e)–7(l) over a 4 s time trace ($680\tau_{\text{conv}}$), with actuation applied at $t = 0$. First, the single-jet actuation is analyzed in detail in Figs. 11(a)–11(h)

(control is applied using jet 1 rather than jet 3 in Fig. 10), which leads to an attitude bias in $-\alpha_y$ and $+\alpha_z$ and can be clearly observed in Figs. 11(a) and 11(e), with the model wake having a bias in $+y$ and $+z$ by ~ 10 mm each. The time evolution of the U_x velocity for the single-jet actuation shows a reduction of the wake oscillation by $\sim 40\%$ at $t = 340\tau_{\text{conv}}$ and $\sim 70\%$ at $t = 510\tau_{\text{conv}}$ in the horizontal direction [Fig. 11(a)], while the oscillation amplitude does not noticeably change in the vertical direction [Fig. 11(e)]. This development of the wake deficits in the horizontal and vertical directions is comparable with the development of the yaw and pitch angular velocities [compare Fig. 11(a) with Fig. 10(b) and Fig. 11(e) with Fig. 10(a)]. The U_y component of the wake velocity in the horizontal centerline is altered by the jets from its initially symmetric distribution by losing its negative v band at $y/D = 0.5$ and gaining a large region of positive v [see Fig. 11(b)]. The actuation also develops a rolling feature in the wake with a $-U_y$ component at $z/D = 0.5$, and a $+U_y$ component at $z/D = -0.5$. This rolling feature is not observed in the horizontal wake centerline, and like the baseline flow, the U_z component of the wake is not significant on the horizontal centerline [cf. Figs. 11(c) and 7(g)]. The U_z component in the vertical direction is like the U_y component in the horizontal direction where it is also dominated by a $+U_z$ component throughout the wake, but this added positive velocity region is added in the inner wake, and the $-w$ band at $z/D = 0.5$ remains intact. The streamwise vorticity ζ_x becomes more organized in the horizontal centerline of the wake [Fig. 11(d)], where the time-dependent oscillations of vorticity develop into a predominantly negative ζ_x at $y/D > 0$, and bands of alternating signs of ζ_x for $y/D < 0$, which are roughly time invariant. Figure 11(h) shows that the structure of ζ_x does not have a significant change in the vertical centerline and primarily is only translated in the $+z$ direction. Next, the open-loop four-jet actuation is shown in Figs. 11(i)–11(p). For this actuation, the oscillation of the location of the wake deficit increases in both y and z , as shown in Figs. 11(i) and 11(m), respectively. The horizontal centerline U_y component shown in Fig. 11(j) shows the introduction of oscillating negative and positive regions with magnitudes larger than the baseline, with a slightly larger positive component attributed to slight mismatches in the strength of the synthetic jet actuators. Like the single jet, the four-jet actuation develops a rolling feature in the wake seen by the $-U_y$ component at $z/D = 0.5$, and a $+U_y$ component at $z/D = -0.5$ in Fig. 11(n). It is noteworthy that the corresponding baseline v component has bands of the same sense and did not have the rolling feature in the vertical centerline [see Fig. 11(j)]. The cross-stream U_z components of the wake in both the vertical and horizontal centerlines are like the baseline flow, with a notable increase in magnitude in the inner wake region [$|y/D| < 0.4$ in Fig. 11(k) and $|z/D| < 0.4$ in Fig. 11(o)]. This trend is also true with the vorticity, seen in Figs. 11(l) and 11(p), where the structure remains like the baseline with an increased magnitude in the inner wake, except this increase is significantly more substantial in the horizontal centerline as opposed to the vertical centerline [compare Fig. 11(l) with Fig. 11(p)].

The POD modes of the wake behind the model with open-loop actuation are calculated using the wake data that were used in Fig. 11 (using 2500 images over a 5 s trace, $850\tau_{\text{conv}}$, or $7.7\tau_z$). The streamwise component of these modes $\bar{\varphi}_{n,u}$ is shown in Fig. 12 for the open-loop single-jet [Figs. 12(a)–12(e)] and four-jet [Figs. 12(f)–12(j)] actuation with $n = 1$ [Figs. 12(a) and 12(f)], $n = 2$ [Figs. 12(b) and 12(g)], $n = 3$ [Figs. 12(c) and 12(h)], and $n = 4$ [Figs. 12(d) and 12(i)], along with the energy contribution of these modes [Figs. 12(e) and 12(j)]. Single-jet open-loop actuation leads to three new streamwise velocity modes that were not observed in the absence of actuation, where the only repeating mode is attributed to the yaw instability [compare Fig. 12(b) with Fig. 8(a)], but this mode now has the second highest energy contribution (dropping from 9% in the baseline to 5.5%), as opposed to the dominant contribution. The new highest energy mode in Fig. 12(a) is most comparable with the unactuated pitch instability mode [Fig. 8(b)], except that the entire mode is rotated by $\sim 45^\circ$, while the top right velocity lobe is severed in a location which coincides with the active jet. The third and fourth modes in Figs. 12(c) and 12(d) are both variations of the unactuated yaw instability mode, with a severed velocity distribution downstream of the active jet, where the difference between these modes is determined by the severed velocity concentration sense, which is either the opposite [Fig. 12(c)] or the same [Fig. 12(d)] as the unactuated mode.

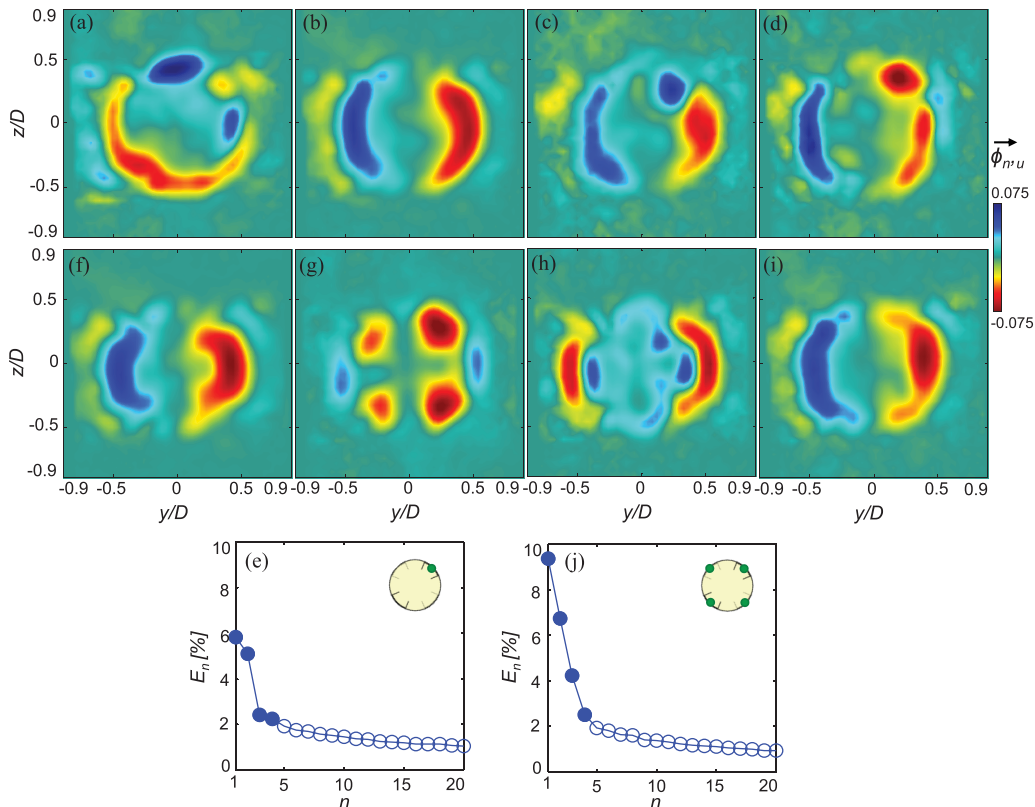


FIG. 12. Contour plots of the streamwise velocity proper orthogonal decomposition (POD) modes $\phi_{n,u}$, with mode number (a) and (f) $n = 1$, (b) and (g) $n = 2$, (c) and (h) $n = 3$, and (d) and (i) $n = 4$, and (e) and (j) the energy distribution of these modes for (a)–(e) open-loop single-jet and (f)–(j) four-jet actuations at $Re_D = 1.62 \times 10^5$.

Compared with the unactuated flow, the 9% energy in the baseline yaw instability is redistributed to three different mode shapes with varying influence by the active jet (modes 2–4), while the pitch mode is energized from 3% to 6%, with a change in shape due to the active jet, becoming a new dominant mode [compare Fig. 12(e) with Fig. 8(h)]. Four-jet actuation compresses the highest energy unactuated mode in the z direction [Fig. 12(f)] and increases its energy percentage of the flow [see Figs. 12(e) and 12(j)]. In addition, a secondary mode that resembles the highest energy baseline mode appears as mode 4 [compare Fig. 12(i) with Fig. 8(a)]. Mode 2 [Fig. 12(g)] and mode 3 [Fig. 12(h)] are two new modes that are not present in the unactuated flow and are attributed to continuous jet actuation, where mode 2 shows a four-lobe distribution downstream of the active jets (with an additional velocity concentration in the $\pm y$ extremes, attributed to the oscillation of the model). The shape of mode 3 has a central lobe that is concave at the location of the jets, surrounded by an external velocity distribution of opposing sense in the $\pm y$ direction but absent in the $\pm z$ direction. The energy distribution after applying the four-jet control has some differences from the baseline energy distribution [compare Fig. 12(j) with Fig. 8(h)], where it introduces two new high-energy modes (mode 2 and 3) and has more energy in its yaw fluctuations (between modes 1 and 4), which is commensurate with the slight model yaw oscillation growth upon actuation observed in Figs. 10(d), 10(h), and 11(i).

To characterize the new dynamic states of the model achieved with open-loop actuation (beyond the transitory state), multiple different open-loop actuation programs are applied. These programs

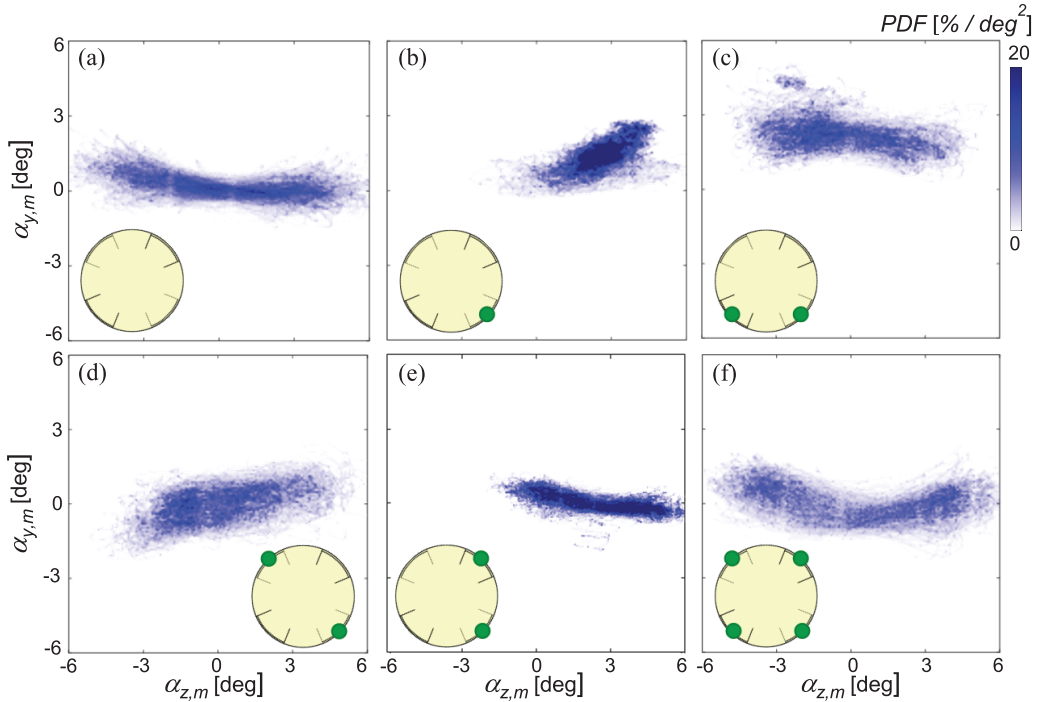


FIG. 13. Spatial probability density functions of flow-induced dynamics of the model over 25 instantaneous measurements of $680\tau_{\text{conv}}$ for (a) the unactuated flow along with actuation by (b) open-loop single-jet, (c) two adjacent jets in the pitch direction, (d) two opposite jets, (e) two adjacent jets in the yaw direction, and (f) four-jets, at $\text{Re}_D = 1.62 \times 10^5$.

are recorded over 25 instantaneous traces, each at $t = 340\tau_{\text{conv}}$ to $1700\tau_{\text{conv}}$ following the onset of actuation ($3400\tau_{\text{conv}}$ total data), and the data are binned into a probability density function of the realized model yaw and pitch coordinates, which is the same as in Figs. 5(k) and 5(l). Five open-loop actuation programs are investigated in Fig. 13: single jet [Fig. 13(b)], two adjacent jets in the pitch direction [Fig. 13(c)], two opposite jets [Fig. 13(d)], two adjacent jets in the yaw direction [Fig. 13(e)], and four jets [Fig. 13(f)]. Figure 13(a) shows the flow in the absence of actuation using the data in Fig. 5(k) and is included for reference. The application of single-jet control shown in Fig. 13(b) biases the motion by $\sim 2^\circ$ yaw and 1.5° in pitch and reduces the oscillation by $\sim 60\%$ [in agreement with Figs. 10(b) and 11(a)], and this offset direction depends on which jet is activated [jet 3 is active in Fig. 13(b)], where different offsets can be implemented by utilization of different jets. Upon activation of the lower two jets [jets 2 and 3, Fig. 13(c)], the model becomes biased at $\sim 2.5^\circ$ in pitch and centered in yaw, while its yaw oscillations are reduced by 20%, and its pitch oscillations are increased by 5%. When the right-side jets are active [jets 1 and 3, Fig. 13(e)], the model becomes biased at $\sim 2.5^\circ$ in yaw, while remaining approximately centered in pitch, and its oscillation amplitude is reduced by 40% in both yaw and pitch. Figure 13(d) shows the effect of two opposing actuators (jets 3 and 4), where the actuation effectively rotates the α_y with α_z response (the slope changes from -0.23 to $+0.31$, compare Fig. 13(a) with Fig. 13(d)], but the yaw amplitude is only reduced 25%, while the pitch amplitude is not significantly altered. Finally, four-jet actuation has a slightly detrimental response, increasing the oscillation amplitudes in yaw and pitch by ~ 5 and 10% , respectively [in agreement with the data shown in Figs. 10(c), 10(d), 10(g), and 10(h), and Figs. 11(i)–11(p)]. The induced dynamics in Figs. 13(d) and 13(f) show that the effects of open-loop actuation on the dynamics of the model are less pronounced when the active jets are opposite to each other.

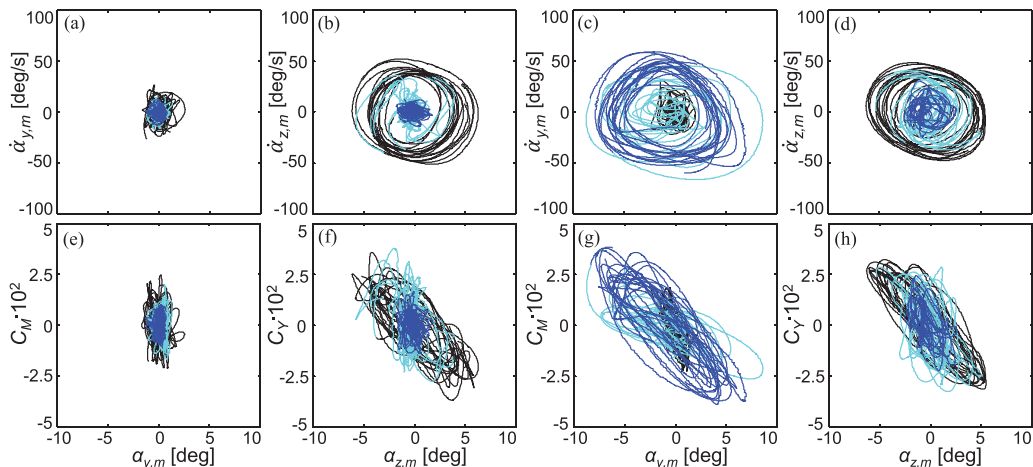


FIG. 14. Phase plots of closed-loop actuations: (a), (b), (e), and (f) hold center and (c), (d), (g), and (h) amplify pitch presented in the same fashion as the data in Fig. 10, using a maximum $C_\mu = 0.003$.

VI. CLOSED-LOOP CONTROL OF THE PRECESSING BODY

For this 3-DOF model, a closed-loop coupled proportional-integral-derivative (PID) feedback controller was designed to provide command signals to the synthetic jets, as discussed in detail in Appendix. It is noted that, while none of the jets are aligned with the two primary directions (pitch and yaw), the flow control scheme distributes control inputs to the jets commanding individual momentum jet coefficients, regardless of the roll angle of the model, to effect the desired pitch and yaw response. The effect of this closed-loop feedback driven controller is initially examined at $U_o = 28$ m/s ($Re_D = 1.62 \times 10^5$) with two different control algorithms aimed at the two main aims of attaining a given model attitude or effecting an oscillatory motion, namely, holding the model at center and to amplify its pitch. Figures 14(a), 14(b), 14(e), and 14(f) show the flow controller activated with a goal of holding the model at $\alpha_y = \alpha_z = 0^\circ$, and Figs. 14(c), 14(d), 14(g), and 14(h) show the control goal of amplifying the pitch motion, with phase plots of the pitch [Figs. 14(a) and 14(c)] and yaw [Figs. 14(b) and 14(d)] rates and pitch [Figs. 14(e) and 14(g)] and yaw [Figs. 14(f) and 14(h)] moments. Upon activation of the hold-center control, the model achieves a new state of $\pm 1^\circ$ in both pitch and yaw within ~ 0.1 s ($\sim 0.15\tau_z$ or $17\tau_{conv}$) regardless of where the control started in the motion cycle of the model. This is equivalent to a reduction of the model oscillation by 35% in pitch [Fig. 14(a)] and 83% in yaw [Fig. 14(b)]. The commensurate moments, C_M and C_Y , are each reduced to ± 0.015 or an equivalent reduction of 33% [Fig. 14(e)] and 50% [Fig. 14(f)], respectively. For the pitch amplification objective [Figs. 14(c), 14(d), 14(g), and 14(h)], the resulting controlled motion has the interesting feature that $\dot{\alpha}_y$ and C_M begin to resemble a larger amplitude version of the unactuated $\dot{\alpha}_z$ and C_Y [compare the actuated traces in Figs. 14(c) and 14(g) with the unactuated in Figs. 14(d) and 14(h)]. Furthermore, the controlled yaw response during pitch amplification resembles the uncontrolled pitch response [compare the actuated traces in Figs. 14(d) and 14(h) with the unactuated in Figs. 14(c) and 14(g)]. The combination of these two control algorithms shows that, with appropriate feedback control, the direction of the baseline instability in this model can be effectively rotated or minimized.

The time-domain response of the model trajectory and the feedback control commands for a single instantaneous trace in the hold-center control depicted in Figs. 14(a), 14(b), 14(e), and 14(f) is shown in Fig. 15 as an illustration of the control sequence. The transient responses of α_x , α_y , and α_z are presented in Figs. 15(a)–15(c), respectively, with the commensurate jet momentum coefficient commands for jets 1–4 presented in Figs. 15(d)–15(g), respectively, before actuation

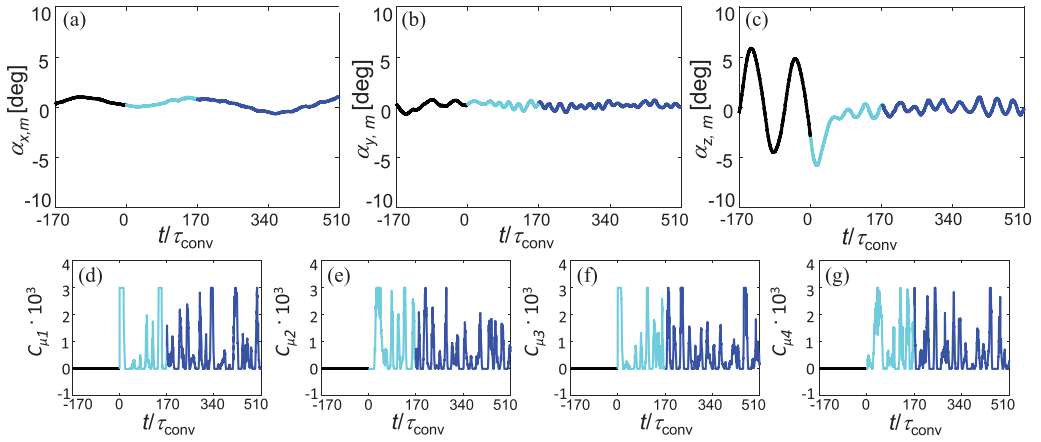


FIG. 15. Time history plots of hold-center closed-loop actuation with measured model (a) roll, (b) pitch, and (c) yaw and output jet momentum coefficients C_μ for (d)–(g) jets 1–4, respectively.

onset in black, transient dynamics in cyan, and controlled dynamics in blue. Upon actuation onset, the yaw amplitude [Fig. 15(c)] is immediately diminished, reducing from $\sim 5^\circ$ to 1° at $\sim 85\tau_{\text{conv}}$, and this diminished amplitude is also accompanied by a decreased period from $\sim 100\tau_{\text{conv}}$ to $40\tau_{\text{conv}}$. For the pitch in Fig. 15(c), there is a similar effect as in yaw, with a decrease of amplitude from $\sim 1^\circ$ to 0.5° with an increase of frequency from $50\tau_{\text{conv}}$ to $20\tau_{\text{conv}}$. Interestingly, Fig. 15(a) indicates a small increase in roll amplitude from 0.5° to 1° , biasing the roll response back toward the roll-zero position, with no noticeable change in frequency. It is asserted this roll behavior is not a response to jet control but a natural aperiodic variation in roll similar to in unactuated pitch and yaw because its frequency is an order of magnitude lower than any frequency applied by the jet momentum coefficients [compare Fig. 15(a) with Figs. 15(d)–15(g)]. The synthetic jet momentum coefficients shown in Figs. 15(d)–15(g) show an initial square wave command in jets 1 and 3 to impart a moment in $+\alpha_z$ to slow the yaw rate down. At $\sim 20\tau_{\text{conv}}$, the commands to jets 1 and 3 reduce dramatically, and the commands to jets 2 and 4 saturate to impart $-\alpha_z$ to slow the yaw rate down until it is captured near zero (at $\sim 70\tau_{\text{conv}}$). Afterwards, the blue traces in Figs. 15(d)–15(g) do not show an obvious pattern in the jet commands, where they are mostly higher-frequency commands which the flow controller produces to reject any pitch or yaw rates that would move the model away from center [with a period of $\sim 20\tau_{\text{conv}}$, on the same order as the pitch response of the model in Fig. 15(b)].

The evolution of the near wake upon the onset of the closed-loop actuation shown in Figs. 14 and 15 is analyzed in detail in Fig. 16, with the PIV-measured time development of the wake centerlines presented in Figs. 16(a)–16(h) and Figs. 16(i)–16(l) for hold-center and pitch-amplification control cases, respectively. These data are presented in a similar fashion to the data for open-loop actuation in Figs. 11(a)–11(l). For the hold-center actuation, the horizontal and vertical wake deficits shown in Figs. 16(a) and 16(e) are immediately transitioned into a higher-frequency response of ~ 4 Hz, where the extent of the horizontal oscillation is significantly reduced, with a slight increase in the vertical extent. This higher-frequency response continues in the cross-stream velocities U_y and U_z , which have a similar actuation structure to the baseline flow, with a much higher periodic frequency [compare Figs. 16(b), 16(c), 16(f), and 16(g) with Figs. 7(f), 7(g), 7(j), and 7(k)]. It is also important to note that this control restores symmetry to the flow, where the actuation-induced horizontal centerline U_y resembles the vertical centerline U_z [compare Fig. 16(b) with Fig. 16(g)], and the horizontal centerline U_z resembles the vertical centerline U_y [compare Fig. 16(c) with Fig. 16(f)], which is expected when the model is centered and not moving due to its azimuthal symmetry. This trend is consistent for the streamwise vorticity ζ_x , where both the horizontal and vertical centerlines show similar traces, each with an inner-wake region full of rapidly oscillating,

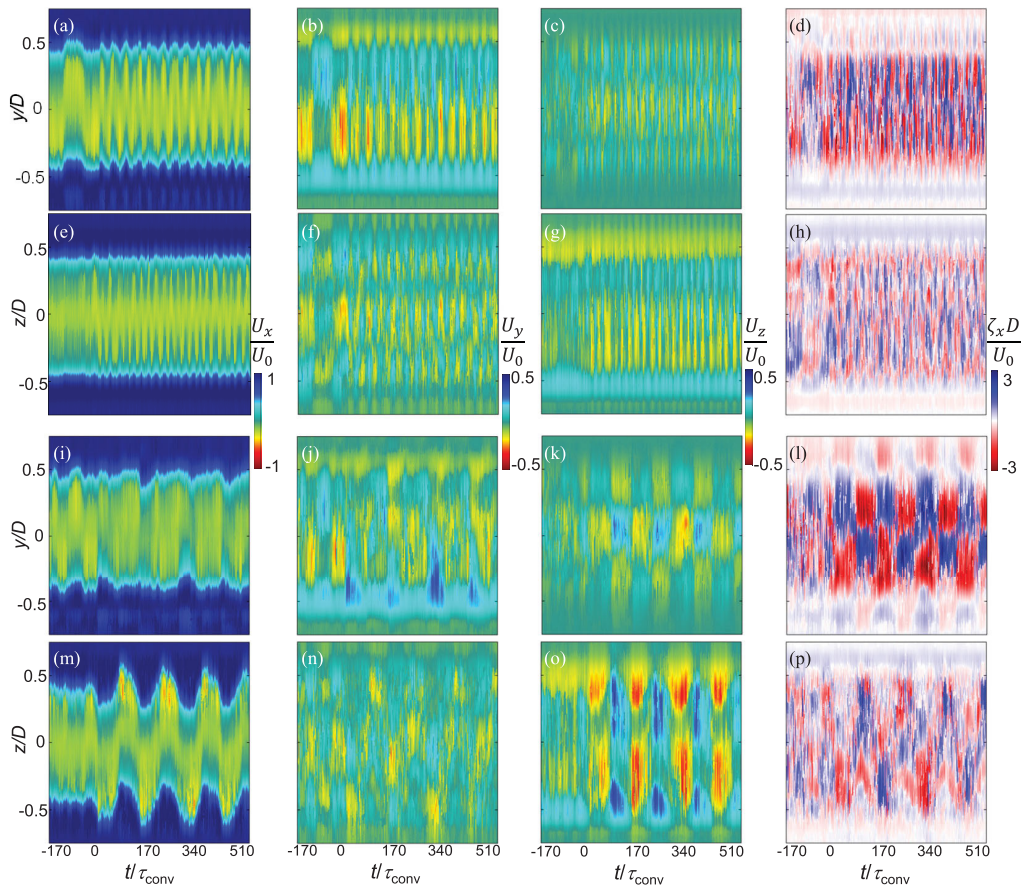


FIG. 16. The time development of the wake for the closed-loop control algorithms (a)–(h) hold center and (i)–(p) amplify pitch presented in the same fashion as the data in Fig. 11, using a maximum $C_{\mu} = 0.003$.

low-amplitude concentrations of vorticity, and the outer wake having a weak band structure [compare Fig. 16(d) with Fig. 16(h)]. The structure of the wake with closed-loop, hold-center actuation is also in excellent agreement with low-speed SPIV velocity and vorticity time traces measured on a static centered model at a downstream location of $x/D = 1$ (these data are presented in a different study by Lambert *et al.* [20]). In the presence of pitch amplification control [Figs. 16(i)–16(p)], the original oscillations over the wake deficit are horizontally reduced [Fig. 16(i)], while new vertical oscillations are introduced with a larger magnitude than the unactuated yaw oscillations [compare Fig. 16(m) with Fig. 7(e)]. In addition, the U_z velocity throughout the centerlines has a larger amplitude than the U_y velocity [compare Figs. 16(k) and 16(o) with Figs. 16(n) and 16(j)], with the highest amplitude oscillation introduced in the actuated vertical centerline U_z component, which resembles the same structure as the baseline U_y component [compare Fig. 16(o) with Fig. 7(f)]. The horizontal and vertical ζ_x fluctuations associated with pitch amplification now resemble the unactuated vertical and horizontal fluctuations, respectively, with the exception that the magnitude of the actuated ζ_x in the wake throughout the horizontal centerline has a more significant magnitude [compare Fig. 16(l) with Fig. 7(i) and Fig. 16(p) with Fig. 7(h)]. The significance in these wake measurements is that the actuation for pitch amplification effectively switches the yaw dynamics and the pitch dynamics in the wake (equivalent to switching the horizontal and vertical

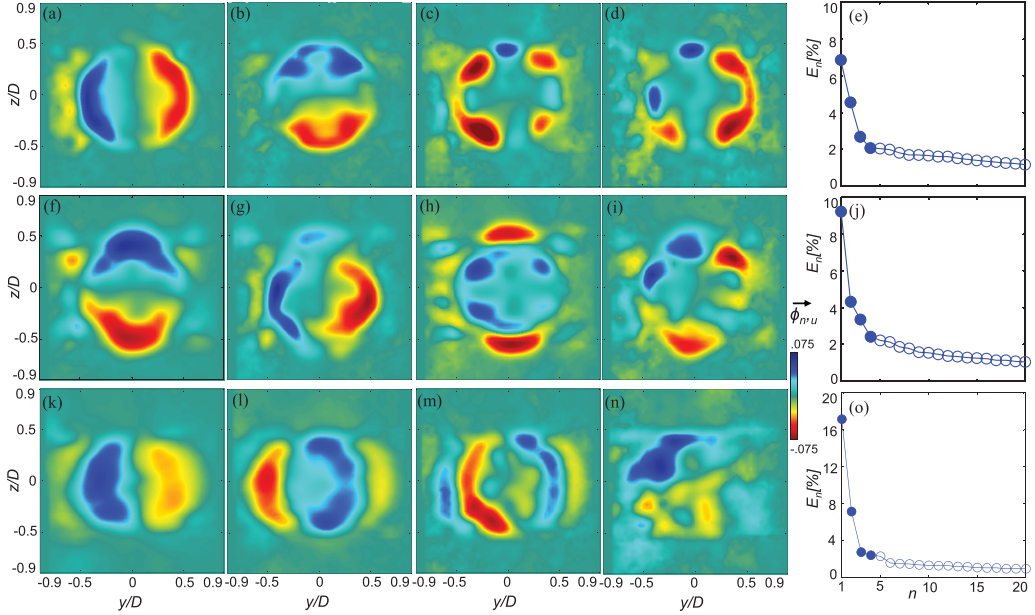


FIG. 17. Contour plots of the streamwise velocity proper orthogonal decomposition (POD) modes $\phi_{n,u}$, with mode number (a), (f), and (k) $n = 1$, (b), (g), and (l) $n = 2$, (c), (h), and (m) $n = 3$, and (d), (i), and (n) $n = 4$, and (e), (j), and (o) the energy distribution of the modes for $\text{Re}_D = 1.62 \times 10^5$, for (a)–(e) closed-loop oscillation suppression, (f)–(j) pitch amplification, and (k)–(o) yaw amplification.

centerline measurements), which is commensurate with the switched yaw and pitch motions and moments measured in Figs. 14(c), 14(d), 14(g), and 14(h).

The respective POD modes of the wake behind the model with closed-loop actuation are calculated using the wake data in Fig. 16 (a set of 2500 images for a 5 s trace, $850\tau_{\text{conv}}$, or $7.7\tau_z$), equivalent to the open-loop actuation POD modes in Fig. 12. The streamwise component of these modes $\bar{\varphi}_{n,u}$ is shown in Fig. 17 for the hold-center [Figs. 17(a)–17(e)] and pitch-amplification [Figs. 17(f)–7(j)] closed-loop actuations already discussed in Figs. 14 –16 as well as an additional closed-loop actuation goal for yaw amplification [Figs. 17(k)–17(o)]. The first four modes are shown in Fig. 17 with $n = 1$ [Figs. 17(a), 17(f), and 17(k)], $n = 2$ [Figs. 17(b), 17(g), and 17(l)], $n = 3$ [Figs. 17(c), 17(h), and 17(m)], and $n = 4$ [Figs. 17(d), 17(i), and 17(n)], along with the energy distribution of these actuated flows [Figs. 17(e), 17(j), and 17(o)]. The hold-center actuation changes the baseline modes significantly, restoring symmetry between the first and second modes in pitch and yaw [compare Figs. 17(a) and 17(b) with Figs. 8(a) and 8(b)]. In addition, the energy between these modes is more evenly distributed, changing from 9 and 3% without actuation to 7 and 5% with the hold-center actuation, as shown in Fig. 17(e). Modes 3 and 4 were not present in the baseline flow and resemble mode 2 from the open-loop all-four actuation [compare Figs. 17(c) and 17(d) with Fig. 12(g)]. The key difference between the closed-loop hold-center and the open-loop all-four modes is that the effects of the jets result in an asymmetric pair with a larger effect on the left [Fig. 17(c)] and right [Fig. 17(d)] sides, respectively. This paired asymmetry in these two modes represent left and right fluctuations introduced by the controlled closed-loop actuation to oppose the natural yaw instability of the model, and it is hypothesized that the open-loop four-jet actuation was not able to reduce the unactuated yaw oscillation because it did not have significant asymmetric wake dynamics in the cross-stream direction to induce an opposing yawing moment. Application of the pitch amplification switches the energy contribution of the first and second modes of the baseline flow [Figs. 17(f) and 17(g)] from 9 and 3% to 5 and 9%, respectively [Fig. 17(j)].

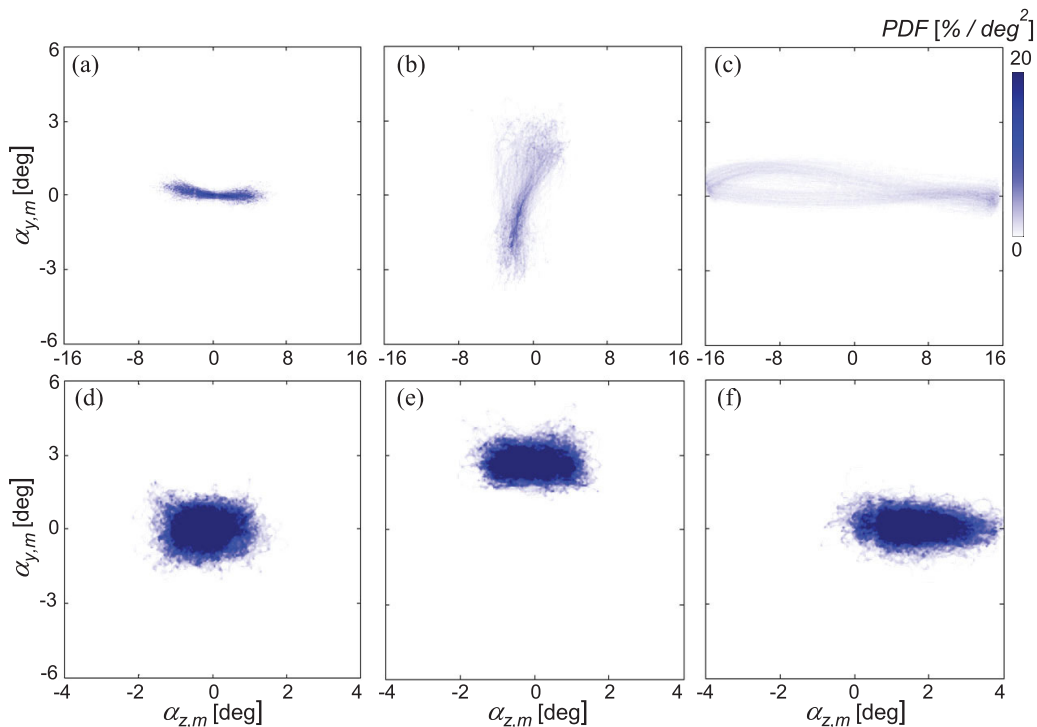


FIG. 18. Spatial probability density functions of flow-induced dynamics of the model for closed-loop actuations: (a) unactuated, (b) amplify pitch, (c) amplify yaw, (d) hold center, (e) hold pitch up, and (f) hold yaw left presented in the same fashion as the data in Fig. 13.

This switch of the pitch and yaw instabilities is commensurate with the switch in forces and wakes discussed in both Figs. 14(c), 14(d), 14(g), and 14(h) and Figs. 16(i)–16(p). In addition, the new third and fourth modes introduced by actuation have not been observed in previous actuation programs and primarily extend in the pitch direction with either a symmetry in the yaw direction [mode 3, Fig. 17(h)] or a weak antisymmetry in the yaw direction [mode 4, Fig. 17(i)]. The third closed-loop controller objective is a yaw amplification actuation which is like the pitch amplification. Upon yaw amplification control, the structure of the unactuated pitching mode is rotated and diffused, and its energy is dropped from the second to the fourth mode [Fig. 17(n)]. The three highest modes that are present are all preferentially in the yaw direction, with the first mode being the equivalent of the unactuated first mode [Fig. 17(k)]. Mode 2 in yaw amplification is a rotated version of mode 3 in pitch amplification [compare Fig. 17(l) with Fig. 17(h)], while a new mode 3 is introduced that appears to be excitation of the roll of the model [Fig. 17(m)]. This new closed-loop control significantly increases the energy in the yaw modes from 9% to a total of 27%, split across three modes, while reducing the energy of all the other measured modes, as shown in Fig. 17(o).

Furthermore, two new actuation programs that use only two adjacent synthetic jet actuators for trajectory control are introduced for which the controller uses only derivative feedback to oppose the natural oscillations of the model. In these programs, the model reaches equilibrium when the nominal aerodynamic force induced by an active jet balances the flow-induced aerodynamic force. The control programs utilize either jets 1 and 3 (denoted as hold left), to hold the model in positive yaw (nose to the left), or jets 2 and 3 (denoted as hold up), to hold the model in positive pitch (nose up). Figure 18 shows probability density functions of the closed-loop actuated model dynamics (the data recording is the same as in the open-loop actuations in Fig. 13). Amplification of the pitch or yaw [Figs. 18(b) and 18(c), respectively] yield $(\pm 8.5^\circ, \pm 2.5^\circ)$, or $(\pm 1.9^\circ, \pm 16.2^\circ)$ in (pitch,

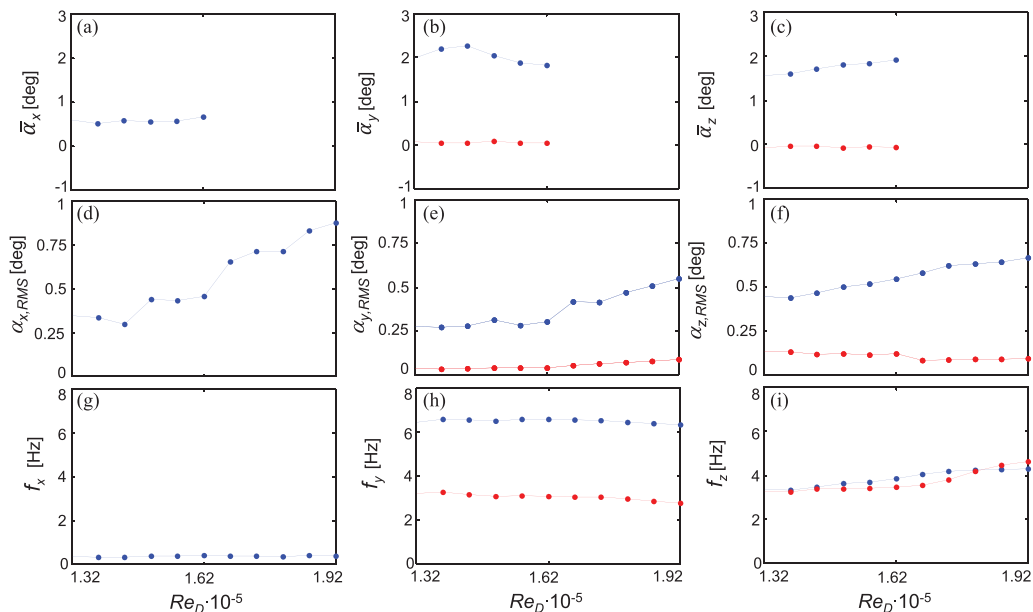


FIG. 19. Model (blue) and sting (red) closed-loop control induced maximum deflections with (a)–(c) hold-right or hold-up actuations, (d)–(f) hold-center root mean square (RMS) amplitude, and (g)–(i) hold-center characteristic frequency in the (a) and (d) roll, (b) and (e) pitch, and (c) and (f) yaw directions, with Reynolds number.

yaw), respectively. The motion data for the base flow [$\pm 1.5^\circ$ pitch and $\pm 5.5^\circ$ yaw, and the same data as in Fig. 5(k)] are plotted in Fig. 18(a) for reference. Figure 18(d) shows the closed-loop hold-center actuation with a fluctuation of $\pm 1^\circ$ in both pitch and yaw around its goal of 0° . Both the hold-left and hold-up actuations cause a similar fluctuation with different offsets: $\pm 1.5^\circ$ yaw and $\pm 0.6^\circ$ pitch around an offset 2° pitch [Fig. 18(e)], and $\pm 1.6^\circ$ yaw and $\pm 0.8^\circ$ pitch around an offset 2° yaw [Fig. 18(f)], respectively. For these new stabilized body states, the closed-loop control reaches its new established state in < 0.2 s ($\sim 0.3\tau_z$ or $34\tau_{\text{conv}}$) after activation, with the hold-center actuation having the fastest transient of ~ 0.15 s ($\sim 0.23\tau_z$ or $25\tau_{\text{conv}}$). Figures 18(e)–18(f) demonstrate that the model can be controlled to a preferential angle (with about $\pm 1^\circ$ of high-frequency fluctuation) at 2° pitch or yaw (hold up and hold left) with two adjacent jets, suggesting that alternative control can easily be attained using the other two combinations of adjacent jets for hold right and hold down. Intermediate attitudes can then, in principle, be achieved by using a weighted superposition of these four control programs. For example, equal weights would yield the hold-center command shown in Fig. 18(d) (although there would be slightly larger error due to the lack of proportional control). It should be noted that, even if the model was excited in roll, it could still be controlled in the same manner, although the model would stabilize in the direction that corresponds to the midpoint of the two active jets (not necessarily in pure pitch or in yaw, depending on the roll angle). The combination of these control algorithms shows an ability to induce transient steering in a controlled direction [Figs. 18(b) and 18(c)] or effectively stabilize the model [Figs. 18(d)–18(f)].

Closed-loop stabilization control of the model [cf. Figs. 18(d)–18(f)] is assessed next for varying wind speeds, $1.32 \times 10^5 < Re_D < 1.92 \times 10^5$ [Fig. 19]. These closed-loop control programs are characterized by the maximum average offset value following either hold-up or hold-left actuation [$\bar{\alpha}_x$, $\bar{\alpha}_y$, and $\bar{\alpha}_z$ in Figs. 19(a)–19(c)], the RMS oscillations when applying the hold-center actuation [$a_{x,RMS}$, $a_{y,RMS}$, and $a_{z,RMS}$, in Figs. 19(d)–19(f)], and their hold-center oscillation frequencies [f_x , f_y , and f_z , in Figs. 19(g)–19(i)]. These data are calculated from 25 instantaneous $1360\tau_{\text{conv}}$

time traces [the same number of samples as in Figs. 18(d)–18(f)] with the model roll, pitch, and yaw in blue and sting pitch and yaw in red. When the model is held at a fixed offset angle, the roll offset (0.5°) is approximately invariant with Re_D [Fig. 19(a)], the pitch offset (2.0°) decreases with Re_D [Fig. 19(b)], and the yaw offset (1.8°) increases with Re_D [Fig. 19(c)]. It is noted that the offset angle actuations are not applied for $Re_D > 1.62 \times 10^5$. The RMS oscillations of model pitch for hold center show a reduction of the oscillation to 0.25° at $Re_D = 1.32 \times 10^5$ and to 0.55° at $Re_D = 1.92 \times 10^5$, with corresponding reductions of 50–65% from the motion of the model in the absence of actuation [cf. Figs. 19(e) and 6(b)]. Similarly, the RMS oscillations of model yaw for hold center show a reduction of the oscillation to 0.45° at $Re_D = 1.32 \times 10^5$ and to 0.70° at $Re_D = 1.92 \times 10^5$, with corresponding reductions of 85–75% from the motion of the model in the absence of actuation [cf. Figs. 19(f) and 6(c)]. The application of closed-loop hold-center actuation also reduces the sting oscillation by 30% at $Re_D = 1.32 \times 10^5$ and 85% at $Re_D = 1.92 \times 10^5$. This control does not have a significant effect on either the roll oscillation [cf. Figs. 19(d) and 6(a)] or on its commensurate characteristic frequency [cf. Figs. 19(g) and 6(d)]. Figure 19(h) shows that application of the hold-center control does not alter the pitch frequency of the sting but more than doubles the model pitching frequency from 3 to 6.6 Hz, effectively forcing the frequency of the model to be a harmonic of the sting frequency. In contrast, both the yaw oscillation frequency of the sting and the model increase twofold at $Re_D = 1.32 \times 10^5$ to a factor of 2.5 at $Re_D = 1.92 \times 10^5$ [cf. Figs. 19(i) and 6(f)], remaining close to the same characteristic frequency at all wind speeds tested.

The results in Figs. 18 and 19 indicate that the current wind tunnel model can be directionally controlled with disturbance rejection within 2° in pitch and yaw. To test the control robustness, the sting is subsequently subjected to a commanded disturbance time-harmonic (2 Hz) trajectory of 2° in pitch and yaw that are 90° out of phase, provided by the wire-mounted traverse. Two different closed-loop actuation programs are applied with the objective of external disturbance rejection. The first program commands the orientation of the model to follow the orientation of the sting (effectively keeping the attitude of the model locked to a target), and the second program commands the model to preserve its orientation (selected to be 0°) regardless of the (changing) orientation of the sting, at $Re_D = 1.62 \times 10^5$ (Fig. 20). The trajectories of the model and sting in the absence of actuation are shown in Figs. 20(a) and 20(d), respectively, and application of the sting-follow control is shown in Figs. 20(b) and 20(e), and the sting-rejection control is shown in Figs. 20(c) and 20(f). It is noted that the commanded sting motions through the wire traverse are selected to be very stiff (the changes in the sting trajectory with application of the flow control programs are small) to emphasize the induced changes in the model dynamics [Figs. 20(d)–20(f)]. The unactuated model dynamic response to the sting disturbance shown in Fig. 20(a) is approximately a superposition of the controlled sting dynamics with the model dynamics when the sting is held center [compare Fig. 20(a) with Figs. 20(d) and 5(k)]. The application of sting-follow control effectively forces the trajectories of the model and sting to be within $\pm 0.5^\circ$ in pitch and yaw [compare Fig. 20(b) with Fig. 20(e)]. The alternative sting-rejection control [Fig. 20(c)] fixes the model attitude to 0° regardless of the orientation of the sting with a fluctuation of $\pm 1.5^\circ$ in yaw and $\pm 1^\circ$ in pitch. Figures 20(b) and 20(c) indicate that this actuation can induce a controlled directional bias of the attitude of the model of $\pm 2^\circ$ in pitch or yaw even when it is subject to external disturbances.

The changes in the wake structure stability and dynamics due to the different closed-loop control scenarios are characterized using snapshot dynamic mode decomposition (DMD). The result yields normalized spatial modes ψ_n , with corresponding frequencies f_n and growth rates a_n . Figure 21 shows a dataset when 999 modes are calculated from 1000 snapshots over $340\tau_{conv}$ for the unactuated flow [Figs. 21(a), 21(e), and 21(i)] and for steady-state closed-loop actuations ($170\tau_{conv}$ after activation): hold center [Figs. 21(b), 21(f), and 21(j)], pitch amplify [Figs. 21(c), 21(g), and 21(k)], and yaw amplify [Figs. 21(d), 21(h), and 21(l)]. Figure 21 shows the variation of mode weight d_n , with mode frequency ($0.48 < f < 240$ with steps of $\Delta f = 0.24$) [Figs. 21(a)–21(d)], along with color raster plots of the streamwise velocity component of representative DMD modes $\psi_{n,u}$. To extract these modes, the velocity field at a given time is concatenated as a vector \vec{X} at time

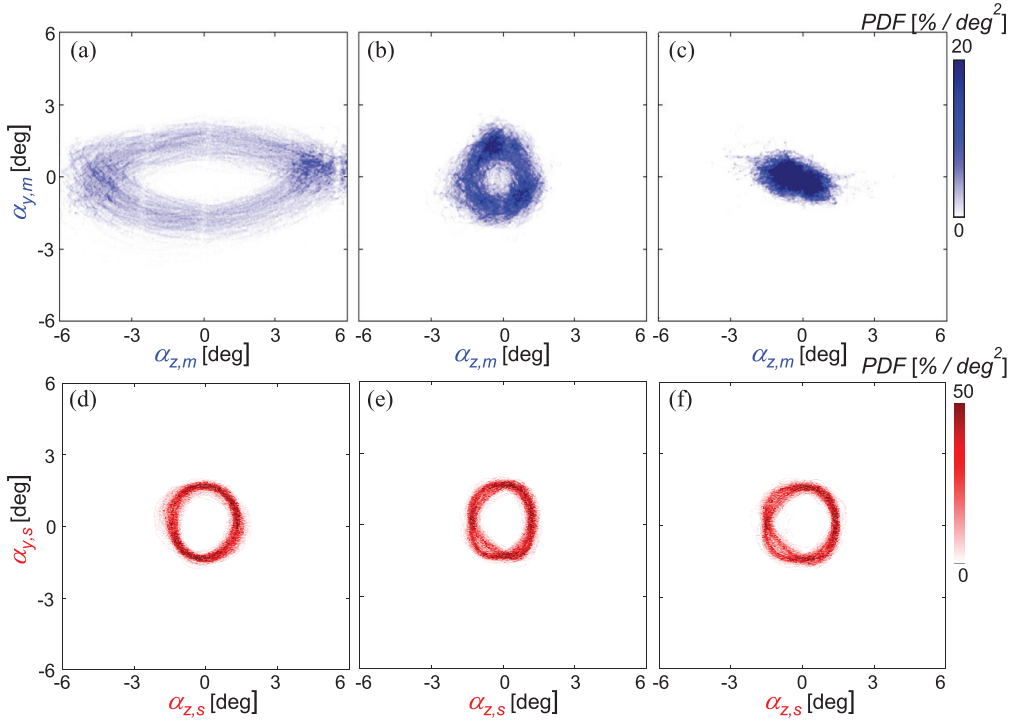


FIG. 20. Spatial probability density functions of (a)–(c) the model (blue) and (d)–(f) sting (red) dynamics over 25 instantaneous measurements of $680\tau_{\text{conv}}$ for (a) and (d) the unactuated flow and closed-loop flow control for the model (b) and (e) to follow the sting motion and (c) and (f) to remain centered independent of the sting motion at $\text{Re}_D = 1.62 \times 10^5$.

t and compared with the field at a subsequent time step \vec{X}' at time $t + \delta t$. A time shift operator A is estimated such that $A\vec{X} \sim \vec{X}'$ for a sequence of snapshots such that its eigenvectors $\vec{\psi}_n$ are the dynamic modes, and the complex eigenvalues $\lambda_{n,\text{dmd}}$ yield estimates of the frequency and growth rate of each mode $f_n = \text{imag}[(\ln(\lambda_{n,\text{dmd}}))/(2\pi\delta t)]$ and $a_n = \text{real}[(\ln(\lambda_{n,\text{dmd}}))/(\delta t)]$, respectively. The time-shift operator is estimated by prefiltering the DMD modes by POD modes, and through this analysis, any DMD mode is a superposition of the POD modes calculated in the dataset. Each dynamic mode is scaled by a weight d_n , such that the sum of all modes reconstructs the first snapshot in the dataset, and thereafter, they change with time depending on their eigenvalues, following Tu [35]: $\sum_1^{N_{\text{set}}} d_n \vec{\psi}_n = \vec{X}|_{t=0}$, $\sum_1^{N_{\text{set}}} d_n \vec{\psi}_n (\lambda_{n,\text{DMD}})^m = \vec{X}|_{t=m\Delta t}$. Because DMD modes are in general not orthogonal, the representative modes are selected such that they are unique, i.e., ψ_1 [Figs. 21(e)–21(h)] is selected for all of them, and a higher representative mode is also selected [Figs. 21(i)–21(l)] that does not encompass the same dynamics (e.g., for the baseline, ψ_2 at $f = 2.16$ Hz is a similar yaw mode to ψ_1 at $f = 1.68$ Hz and is omitted in favor of the pitch mode ψ_3 at 2.88 Hz). The modes are determined by the largest spectral peaks of d_n . In the base flow, ψ_1 (1.6 Hz) and ψ_3 (2.88 Hz), respectively, capture the highest modes of the yaw and pitch instabilities [Figs. 21(e) and 21(i)] and demonstrate that the primary oscillations in the wake are confined to narrow bands within arcs at the outer edges of the wake that scale with the diameter of the bluff body and are like the first two POD modes presented in Figs. 8(a) and 8(b). When hold-center actuation is applied [Figs. 21(b), 21(f), and 21(j)], the spectral components of the yaw and pitch instabilities are attenuated, and two higher spectral components emerge at $f = 4.32$ and 6.72 Hz coupled with the new dominant modes that are nearly symmetric with respect to the y or z axes and

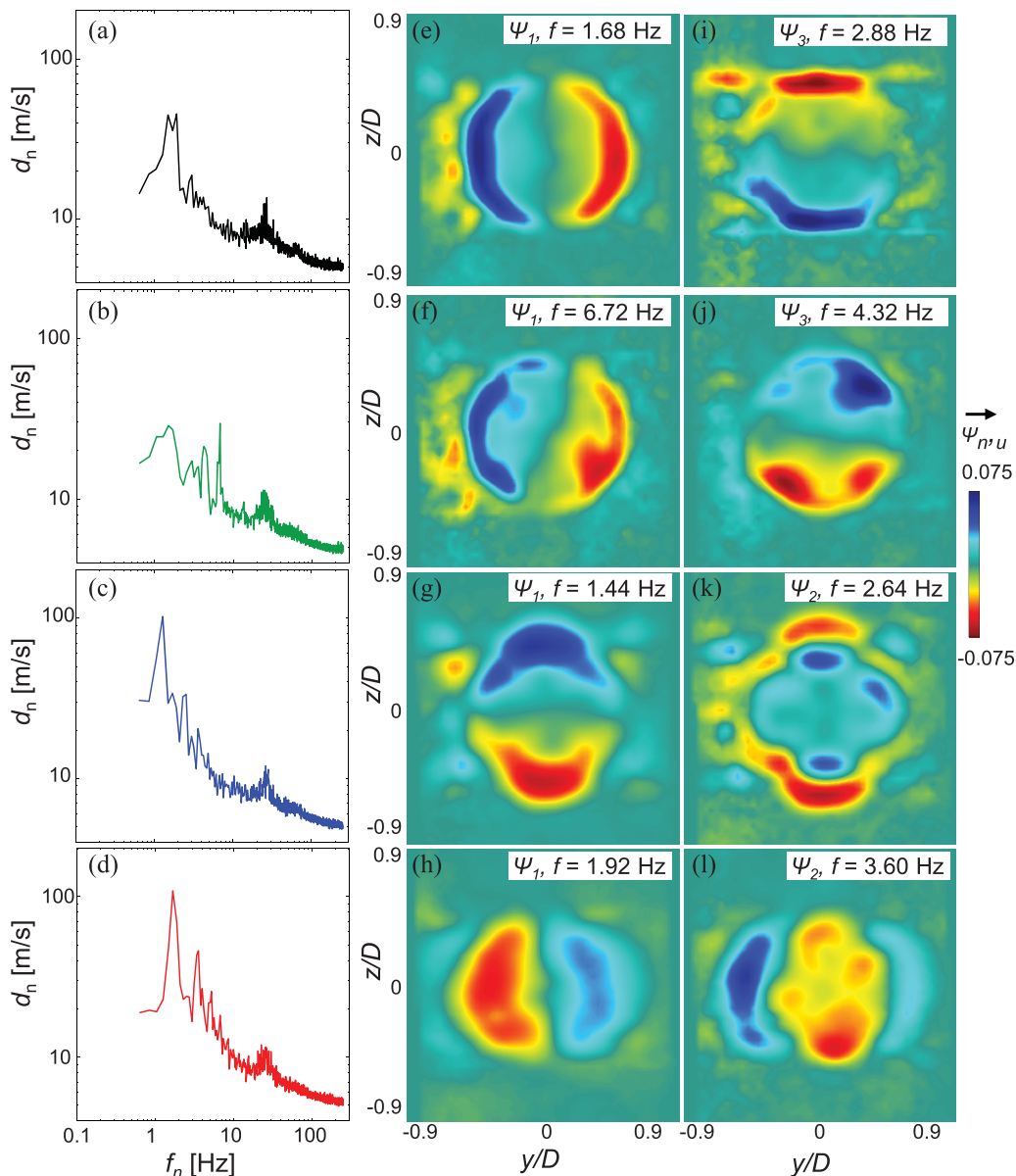


FIG. 21. (a)–(d) Dynamic mode decomposition (DMD) spectral distributions and (e)–(l) color raster plots of the streamwise velocity distributions of dynamic modes $\Psi_{n,u}$ for (a), (e), and (i) the unactuated flow and closed-loop actuation goals: (b), (f), and (j) hold center, (c), (g), and (k) pitch amplify, and (d), (h), and (l) yaw amplify. The mode order (i.e., the n th peak) and respective frequency are noted.

spread more toward the center of the wake as a result of the attenuation of the fluctuation in the attitude of the model. The actuation that leads to amplification of the pitch and yaw excursions of the model are associated with large spectral peaks at (nearly) the frequencies of the instabilities of the base flow with several harmonics appearing [Figs. 21(c) and 21(d)]. While ψ_1 for the pitch and yaw amplification [Figs. 21(g) and 21(h)] is like the corresponding primary yaw and pitch modes in the base flow, the actuated modes spread farther in the direction of excursions and into the center

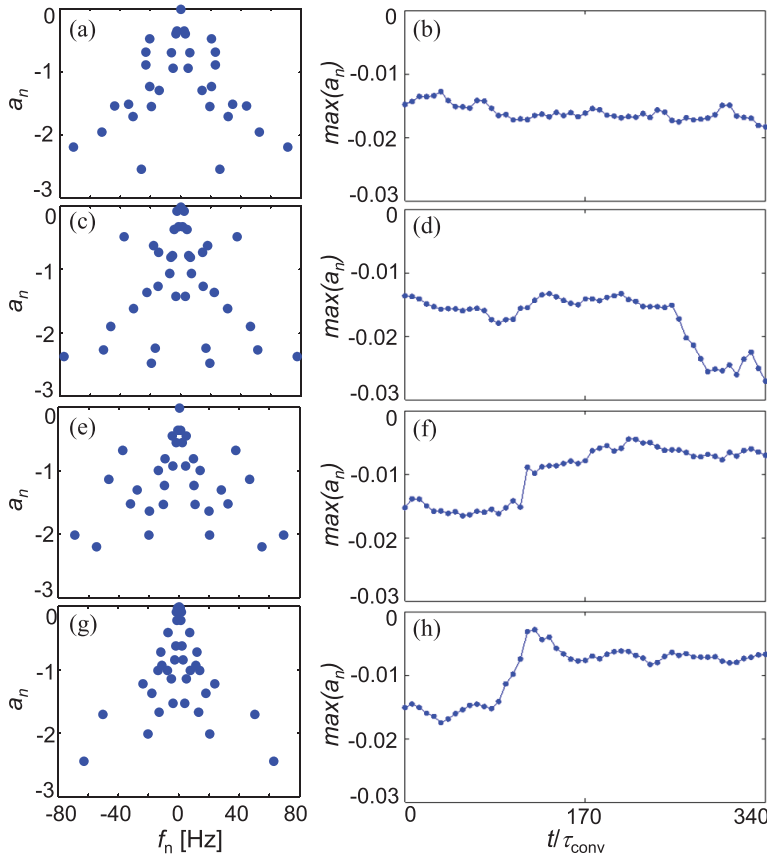


FIG. 22. (a), (c), (e), and (g) Dynamic mode decomposition (DMD) growth rates (40 modes) and (b), (d), (f), and (h) the time development of the growth of the least stable mode within a 2 s ($340 \tau_{\text{conv}}$) interval with actuation starting at $t = 0$, for (a) and (b) the unactuated flow and the actuated closed-loop control for (c) and (d) hold center, (e) and (f) pitch amplify, and (g) and (h) yaw amplify.

of the wake. Furthermore, the higher modes ψ_2 [Figs. 21(k) and 21(l)] have distinct three lobes where the central lobe has the opposite sense of the outer lobes, like the POD modes in Figs. 17(h) and 17(l). Although the DMD modes in Fig. 21 are in principle like the POD modes in Sec. V, these results directly relate the time-dependent spatial variations to the two primary characteristic wake frequencies in pitch and yaw and yield a more intuitive representation.

A unique feature of the DMD analysis is that it enables estimates of the amplification or attenuation of the individual modes. For this analysis, the wake data are prefiltered by the 40 highest energy POD modes ($\sim 50\%$ of the total energy) and the growth rates and frequencies of the 40 largest dynamic modes are computed. Initially, the limit cycle growth rates are plotted [each calculated over the same duration as Figs. 21(a)–21(d)] and are marked along with their respective frequencies in Figs. 22(a), 22(c), 22(e), and 22(g) corresponding to the actuation programs of Figs. 21(a)–21(d) [compare with spatial response in Figs. 18(a), 18(d), 18(b), and 18(c) for unactuated, hold center, pitch amplify and yaw amplify actuation, respectively]. Next, the transient behavior is investigated. For this purpose, this same DMD calculation is carried out within different time windows of the same duration, with the central snapshot of the window varying in time from 1 s before actuation ($-170\tau_{\text{conv}}$) to 1 s afterward ($170\tau_{\text{conv}}$), where the actuation onset is at $t = 0$. In other words, if the central snapshot was at $170\tau_{\text{conv}}$, the data would be the same as in Figs. 22(a), 22(c), 22(e),

and 22(g). The time evolution (plotted using the time of the center of each window) of the least stable mode of each actuation program is plotted in Figs. 22(b), 22(d), 22(f), and 22(h). Clearly, the computation window straddles the unactuated and actuated flows and extends from the pseudostable limit cycle of the base flow to sufficiently long after the actuation, when it reaches a new limit cycle. Therefore, all the modes in this reduced order analysis are semistable (have a negative growth rate). It is noted that a narrower window would better capture the transition associated with the onset of the actuation, and the transition would happen closer to $t = 0$, but the data analysis would be limited by noise in the snapshots. Nevertheless, these findings indicate that the timing of the change in magnitude (attenuation) of the least stable wake mode is in concert with the controlled model dynamics discussed in Sec. V. Namely, the wake instabilities decrease for hold-center actuation [Fig. 22(d)] and increase with the amplification in either pitch or yaw directions [Figs. 22(f) and 22(h)]. This change in the wake stability occurs over 0.15 s, in agreement with the transient closed-loop moments in Fig. 14, although the transition does not occur exactly at the actuation onset ($t = 0$), which is attributed to the effect of the rolling window size in analysis.

VII. CONCLUSIONS

The reciprocal coupled interactions between a forebody-gimbaled axisymmetric bluff body wind tunnel model that is free to precess in pitch, yaw, and roll and the near wake of the body are exploited for prescribing its attitude using fluidic actuation. The flow-induced aerodynamic loads on the model, and thereby its angular attitude, are controlled in a closed loop by fluidic modification of its wake using four independently controlled, aft-mounted synthetic jet actuators. Actuation is applied by azimuthally segmented temporal flow attachment over the tail end of the model and the effects of the induced, transitory changes in the aerodynamic loads are measured by tracking the motion of the model and measuring the commensurate coupled evolution of the flow in the near wake. In the absence of actuation, unstable interactions of the cross-flow with the model in the present range of Reynolds numbers ($\sim 10^5$) lead to natural, nominally time-periodic roll, pitch, and yaw oscillations with some bias toward yaw excursions.

Open-loop modifications of the near wake were first tested to understand its long-term coupling to the angular response of the model using several time-invariant combinations of the actuation jets. These findings were then expanded to exploit the capabilities of active control of the wake of the freely precessing model using a closed-loop PD controller with the measured dynamic attitude of the model as a control input to achieve a desired attitude. In this paper, we demonstrated that closed-loop control of pitch and yaw can significantly attenuate the inherent baseline oscillations of the model by $> 80\%$ over the present range of Re_D within a fraction of the natural oscillation period. In addition to oscillation attenuation, it was also shown that the attitude of the model can be prescribed to steady deflections within $\pm 2^\circ$ in pitch and yaw. Furthermore, it was shown that the control could be tuned to achieve a rapid large-amplitude response and amplify the natural yaw or pitch oscillations by $> 225\%$ of the baseline precession motion.

An important aspect of the effectiveness of the coupled model-wake control approach was also demonstrated by stabilizing the model in the presence of prescribed disturbances that were effected by precessing the support sting by up to $\pm 2^\circ$ in pitch and yaw. It was shown that the controller was able to prescribe a desired model attitude that either tracked the sting motion or nearly decoupled the model from the moving sting using the jet actuation for disturbance rejection. The alteration of the near-wake structure and dynamics in the presence of the closed-loop control was analyzed using DMD of the time-resolved SPIV measurements of the velocity field in the near wake. It was shown that suppression or amplification of the natural oscillations of the model are associated with induced changes in the symmetry of the primary dynamical modes, accompanied by alteration of their spectral content.

These findings indicate that closed-loop control can be adopted to effect time-dependent steering of the attitude of the model and stabilize or destabilize its motion in free flight in the absence of a spin.

ACKNOWLEDGMENT

This paper was supported by the Army Research Office Grant No. W911NF-15-1-0153.

APPENDIX: SYSTEM CONTROL

The designed traverse is controlled through the trajectory tracking controller depicted in Fig. 23. First, the user can provide two command inputs: a time trace for the desired sting trajectory in 5-DOF (all DOFs except roll) and a time trace for flow control actuation commands (e.g., voltage amplitude modulation of the synthetic jet actuator resonance carrier waveforms on the wind tunnel model). Second, the 5-DOF commanded motion is converted into eight servo motor commands (5-DOF to 8-DOF), which are calculated through the geometry of the sting and chosen servo mounting points, assuming the wires are incompressible. The command signal to each servo actuator is then generated using eight PID controllers with the same coefficients [$\kappa_{P,inner} = 4.24$ Nm/rad, $\kappa_{I,inner} = 21.20$ Nm/(rads), and $\kappa_{D,inner} = 0.02$ Nms/rad], which are found from manual iteration and used to command the torque in the motors. Note that, with pure feedback control, there is a phase lag between the desired command and the realized command, so the sting motions are currently restricted to time-periodic motions where optimal PID coefficients yield an output that is self-similar to the desired command with a change in phase and amplitude. The realized motion is then calculated by measuring the conditioned encoder signals and inverting these servo motor positions to the model position using a least squares algorithm (8-DOF to 5-DOF). This control loop is considered the inner loop servo controller in Fig. 23. It is noted that this inner loop controller is

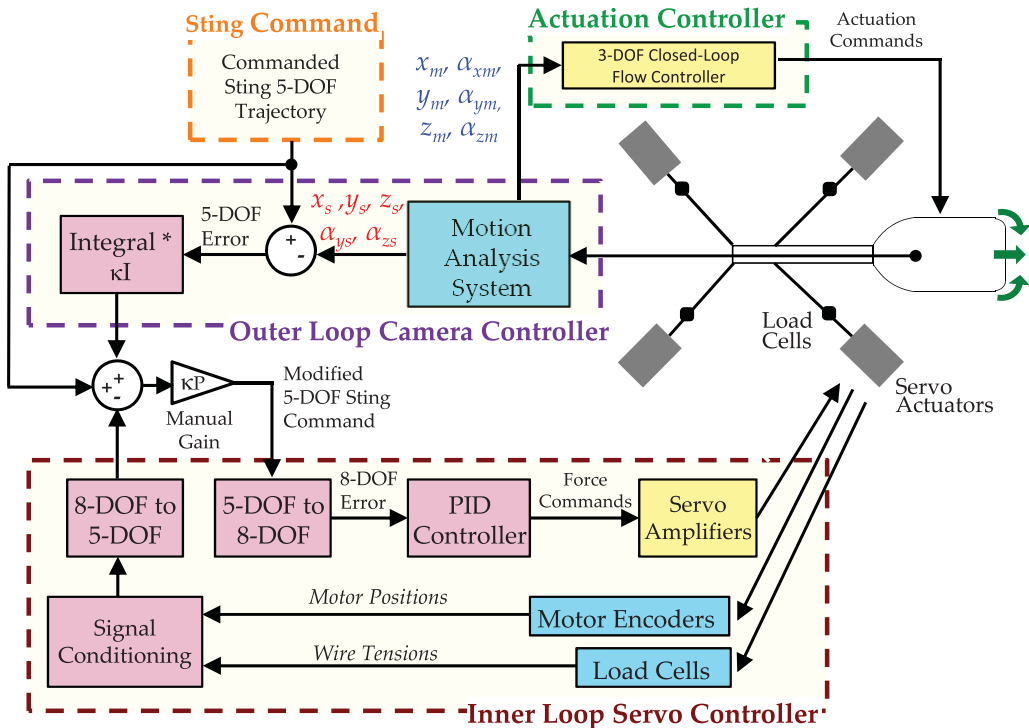


FIG. 23. Schematics of the traverse trajectory tracking controller for measuring and effecting the five degrees of freedom (5-DOF) sting mount and the six degrees of freedom (6-DOF) axisymmetric model; the angular three degrees of freedom (3-DOF) of the axisymmetric model are decoupled and effected solely by flow control.

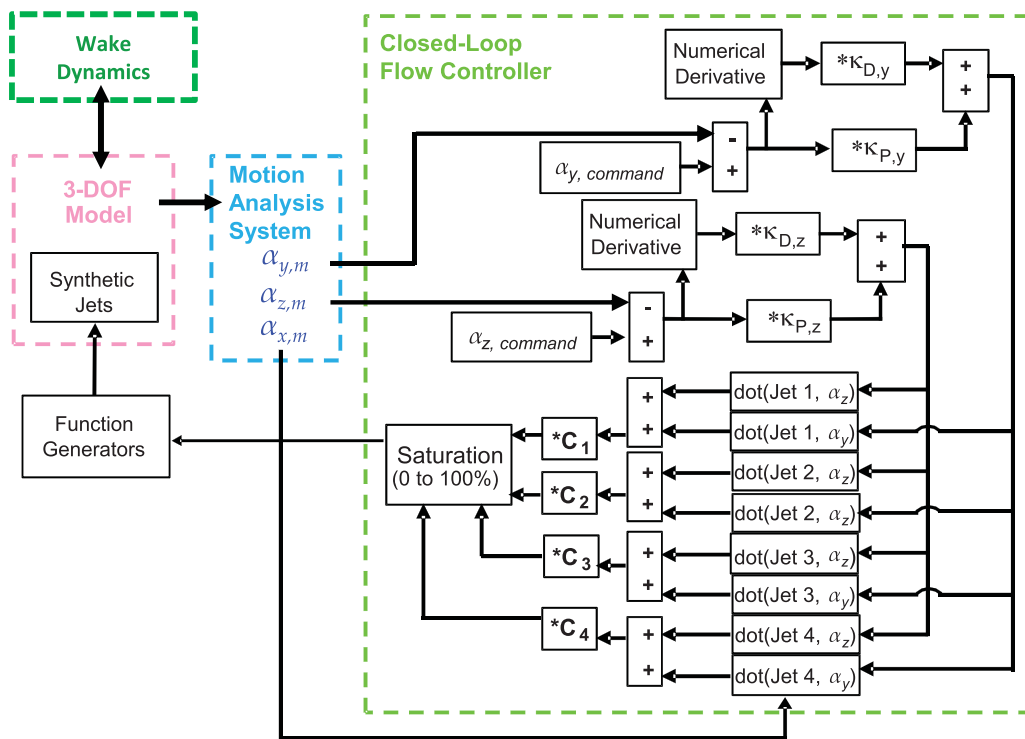


FIG. 24. Schematics of the closed-loop flow controller.

sensitive to errors in the geometric parameters of the traverse (e.g., mounting locations or damping and friction of the motors). To compensate for this geometric model as well as the change in the amplitude of the desired command, an outer loop camera controller shown in Fig. 23 is implemented to adjust the command of the inner loop based on the motion analysis system to allow for accurate trajectory tracking. The outer loop uses an integral error feedback controller that is set such that the measured trajectories reach the desired ones within 10 s ($\kappa_{1,outer} = 0.3/s$ for the 3-DOF translational commands and 0.1/s for the 2-DOF rotational commands). In addition, a manual gain of the inner loop command is implemented, determined by matching the magnitudes of the measured amplitude to the desired amplitude, which depends on the frequency and desired motion. For this paper, only two motions were used: (1) disturbance rejection of any aerodynamic induced vibrations from the flow speed, which is the default command in Secs. III–VII, and (2) commanded time-harmonic (2 Hz) trajectory of 2° in pitch and yaw that are 90° out of phase used for Fig. 20 in Sec. VI.

The actuation controller (shown in the green dotted line in Fig. 23) is shown in detail in Fig. 24. A PD controller is implemented which uses the difference between the command input and actual (camera measured) coordinates ($\alpha_{y,goal}$, $\alpha_{z,goal}$) and (α_y , α_z) as a proportional error for feedback. The derivative of this error is calculated numerically through a low-pass filter. This controller updates at a rate of 1000 Hz (the same update frequency as the wire traverse). Two command signals are created using a weighted superposition with four respective controller coefficients ($\kappa_{D,y}$ and $\kappa_{P,y}$ for pitch and $\kappa_{D,z}$ and $\kappa_{P,z}$ for yaw) to determine the needed magnitudes of actuation in the pitch and yaw directions. These two command signals are then divided into four jet activation signals dependent on the roll angle of the model (for instance, if jets 1 and 3 are aligned with the vertical axis, their activation would only be determined by the pitch command, and the activation of jets 2 and 4 would only be determined by the yaw command), and in general, all four jet activation signals are dependent on both command signals and the roll angle of the model. Additionally, the

relative amplitudes of the jets are also allowed to be scaled by C_1 , C_2 , C_3 , and C_4 coefficients in the controller to correct for their relative maximum jet momentum. These jet signals are then saturated from 0 to 100% (i.e., they can only apply moment in one direction and can never be negative or larger than their maximum expulsion force). The resultant signals are sent as amplitude modulation signals to function generators and corresponding amplifiers (with a fixed carrier frequency of $f_{\text{act}} \approx 1$ kHz, set dependent on flow Reynolds number) to transform each signal into an actuation wave packet for each synthetic jet, where the maximum modulation amplitude corresponds to an output jet momentum coefficient of $C_\mu = 0.003$.

This controller is slightly modified for the hold offset and the amplification control shown in Sec. VI. For the hold-offset control, two jets were disabled (either the pitch negative jets for hold pitch up or the yaw negative jets for hold yaw left). In this mode, the proportional gains ($\kappa_{p,y}$ and $\kappa_{p,z}$) are set to 0, such that the offset pitch or yaw are an equilibrium point the model realizes with only two jets fully stabilizing it, and this offset pitch or yaw then depends on flow speed (as presented in Fig. 19). For the pitch- or yaw-amplification control, a typical PD controller response would be dependent on the magnitude of the desired pitch or yaw command, and therefore, to implement the maximum amplification, the preferred goal (say, pitch) is instead set to 0° , and the controller coefficients determining the pitch motion ($\kappa_{p,y}$ and $\kappa_{D,y}$) are multiplied by -1 , causing the controller to drive the model to its maximum instability in pitch $\sim 0^\circ$. For this amplification, the yaw would still be set to a goal of 0° , with controller coefficients remaining the same for stabilization in that axis. If amplify yaw is implemented instead, the same inversion of the yaw controller coefficients are inverted ($\kappa_{p,z}$ and $\kappa_{D,z}$) while leaving the pitch coefficients the same for stabilization $\sim 0^\circ$.

-
- [1] E. Achenbach, Vortex shedding from spheres, *J. Fluid Mech.* **62**, 209 (1974).
 - [2] E. Berger, D. Scholz, and M. Schumm, Coherent vortex structures in the wake of a sphere and a circular disk at rest and under forced vibrations, *J. Fluid. Struct.* **4**, 231 (1990).
 - [3] T. David, L. Eshbal, V. Rinsky, and R. van Hout, Flow measurements in the near wake of a smooth sphere and one mimicking a pine cone, *Phys. Rev. Fluids* **5**, 074301 (2020).
 - [4] H. V. Fuchs, E. Mercker, and U. Michel, Large-scale coherent structures in the wake of axisymmetric bodies, *J. Fluid Mech.* **93**, 185 (1979).
 - [5] S. J. Lee and P. W. Bearman, An experimental investigation of the wake structure behind a disk, *J. Fluid. Struct.* **6**, 437 (1992).
 - [6] J. R. Calvert, Experiments on the low-speed flow past cones, *J. Fluid Mech.* **27**, 273 (1967).
 - [7] A. M. K. P. Taylor and J. H. Whitelaw, Velocity characteristics in the turbulent near wakes of confined axisymmetric bluff bodies, *J. Fluid Mech.* **139**, 391 (1984).
 - [8] C. Brücker, Spatio-temporal reconstruction of vortex dynamics in axisymmetric wakes, *J. Fluid. Struct.* **15**, 543 (2001).
 - [9] Y. Bury and T. Jardin, Transitions to chaos in the wake of an axisymmetric bluff body, *Phys. Lett. A* **376**, 3219 (2012).
 - [10] D. Fabre, F. Auguste, and J. Magnaudet, Bifurcations and symmetry breaking in the wake of axisymmetric bodies, *Phys. Fluids* **20**, 051702 (2008).
 - [11] P. A. Monkewitz, A note on vortex shedding from axisymmetric bluff bodies, *J. Fluid Mech.* **192**, 561 (1988).
 - [12] H. Oertel Jr, Wakes behind blunt bodies, *Annu. Rev. Fluid Mech.* **22**, 539 (1990).
 - [13] A. Sevilla and C. Martínez-Bazán, Vortex shedding in high Reynolds number axisymmetric bluff-body wakes: Local linear instability and global bleed control, *Phys. Fluids* **16**, 3460 (2004).
 - [14] P. Meliga, D. Sipp, and J.-M. Chomaz, Open-loop control of compressible afterbody flows using adjoint methods, *Phys. Fluids* **22**, 054109 (2010).

- [15] T. Zhu and J. F. Morrison, Simulation of the turbulent axisymmetric bluff body wake with pulsed jet forcing, *Phys. Rev. Fluids* **6**, 124604 (2021).
- [16] J. B. Freund and M. G. Mungal, Drag and wake modification of axisymmetric bluff bodies using Coanda blowing, *J. Aircraft* **31**, 572 (1994).
- [17] K. P. Lo, C. J. Elkins, and J. K. Eaton, Separation control in a conical diffuser with an annular inlet: Center body wake separation, *Exp. Fluids* **53**, 1317 (2012).
- [18] A. R. Oxlade, J. F. Morrison, A. Qubain, and G. Rigas, High-frequency forcing of a turbulent axisymmetric wake, *J. Fluid Mech.* **770**, 305 (2015).
- [19] P. Abramson, B. Vukasinovic, and A. Glezer, Fluidic control of aerodynamic forces on a bluff body of revolution, *AIAA J.* **50**, 832 (2012).
- [20] T. J. Lambert, B. Vukasinovic, and A. Glezer, Aerodynamic flow control of axisymmetric bluff body by coupled wake interactions, *AIAA J.* **56**, 2992 (2018).
- [21] T. J. Lambert, B. Vukasinovic, and A. Glezer, Controlled axisymmetric body-wake coupling in a pitching motion, *Exp. Fluids* **61**, 109 (2020).
- [22] J. McMichael, A. Lovas, P. Plostins, J. Sahu G. Brown, and A. Glezer, Microadaptive flow control applied to a spinning projectile, *AIAA 2004-2512. 2nd AIAA Flow Control Conference* (2004).
- [23] J. Sahu and K. R. Heavey, Unsteady CFD modeling of micro-adaptive flow control for an axisymmetric body, *Int. J. Comput. Fluid D.* **20**, 271 (2006).
- [24] M. Zeidler, E. Garnier, R. Cayzac, and A. Merlen, Fluidic control of a 155 millimeter spin-stabilized projectile using Coanda effect, *AIAA J.* **53**, 1146 (2015).
- [25] R. van Hout, A. Krakovich, and O. Gottlieb, Time resolved measurements of vortex-induced vibrations of a tethered sphere in uniform flow, *Phys. Fluids* **22**, 087101 (2010).
- [26] R. van Hout, A. Katz, and D. Greenblatt, Acoustic control of vortex-induced vibrations of a tethered sphere, *AIAA J.* **51**, 754 (2013).
- [27] T. J. Lambert, B. Vukasinovic, and A. Glezer, A freely yawing axisymmetric bluff body controlled by near-wake flow coupling, *J. Fluid Mech.* **863**, 1123 (2019).
- [28] E. Boujo and O. Cadot, Stochastic modeling of a freely rotating disk facing a uniform flow, *J. Fluid. Struct.* **86**, 34 (2019).
- [29] P. W. Bearman, Vortex shedding from oscillating bluff bodies, *Annu. Rev. Fluid Mech.* **16**, 195 (1984).
- [30] C. H. K. Williamson and R. Govardhan, Vortex-induced vibrations, *Annu. Rev. Fluid Mech.* **36**, 413 (2004).
- [31] C. S. Rinehart, Aerodynamic forces induced by controlled transitory flow on a body of revolution, Ph.D. thesis, Georgia Institute of Technology, 2011.
- [32] E. Lee, Y. Huang, B. Vukasinovic, and A. Glezer, Controlled aerodynamic loads on a slender axisymmetric body at high incidence, AIAA 2021-1943, *AIAA Scitech 2021 Forum* (2021).
- [33] T. J. Lambert, B. Vukasinovic, and A. Glezer, A six degrees of freedom dynamic wire-driven traverse, *Aerospace* **3**, 11 (2016).
- [34] H. Lee, K. Hourigan, and M. C. Thompson, Vortex-induced vibration of a neutrally buoyant tethered sphere, *J. Fluid Mech.* **719**, 97 (2013).
- [35] J. H. Tu, Dynamic mode decomposition: Theory and applications, Ph.D. thesis, Princeton University, 2013.